Journal of Hydrology 610 (2022) 127782

Contents lists available at ScienceDirect

Journal of Hydrology

journal homepage: www.elsevier.com/locate/jhydrol

Research papers

Influence of geological structure on the physicochemical properties and occurrence of middle-deep groundwater in Chongqing, Southwest China

Jieru Zhang [a], Pingheng Yang [a,b,c,*], Chris Groves [c], Xiaohui Luo [d], Yuyang Wang [a]

[a] Field Scientific Observation & Research Base of Karst Eco-environments at Nanchuan in Chongqing, Ministry of Natural Resources, Chongqing Jinfo Mountain Karst Ecosystem National Observation and Research Station, Observation and Research Station of Chongqing Jinfo Mountain Karst Eco-Environments, Ministry of Natural Resources, School of Geographical Sciences, Southwest University, Chongqing 400715, China
[b] Key Laboratory of Karst Ecosystem and Treatment of Rocky Desertification, Ministry of Natural Resources, IRCK by UNESCO, Guilin 541004, China
[c] Crawford Hydrology Laboratory, Department of Earth, Environmental, and Atmospheric Sciences, Western Kentucky University, Bowling Green, KY 42101, USA
[d] China Merchants Ecological Environment Protection Technology Co. Ltd, Environmental Restoration Division, Chongqing 400067, China

ARTICLE INFO

Keywords:
Middle-deep groundwater
Geological structure
Marine sedimentary rock
Karst aquifer
Chongqing, SW China

ABSTRACT

Large marine sedimentary basins often contain concentrated geothermal mineral resources. Chongqing Municipality, located in the Sichuan marine sedimentary basin and the surrounding mountainous area of southwest China, is rich in thermal waters and brines. Chongqing belongs to the Middle-Upper Yangtze Tectonic Block. Previous studies have mostly been based on basin structure, but less on the whole plate structure to study the distribution and evolution of groundwater. In this paper, 78 middle-deep groundwater samples in the study area were collected to better understand the occurrence and hydrochemical evolution of middle-deep groundwater using ionic ratios, hydrogen and oxygen isotopes, and geothermometers. Tectonic stress has been transferred from SE to NW in the Jiangnan Orogenic Belt and from NE to SW in the Qinling-Dabie Orogenic Belt, making the extent of tectonic denudation and its related properties such as hydrochemical type, reservoir temperature, and maximum circulation depth trend along the same directions. Four of the water samples have Br $\times 10^3$/Cl and Na/Cl molar ratios >1.5 and <0.87, respectively, indicating that they are marine metamorphic brines. The ratios of the rest of the samples are mostly distributed in a range suggesting precipitation-dissolved halite or somewhere in between. This suggests that the study area is in the denudation leaching period of the hydrogeological cycle, and the middle-deep groundwater system is still in the dynamic process of formation water (residual metamorphic paleo-seawater) of the previous hydrogeological cycle diluted in places by rainwater. A conceptual circulation model for regional middle-deep groundwater is proposed. Rainfall in the late Pleistocene infiltrated as groundwater recharge via fractures and karst valleys and circulated to deep strata driven by gravity, where it could mix with residual, paleo-evaporated seawater. Then the groundwater was heated by geothermal and chemical energy sources, mixing with shallow groundwater as it moved upward along faults toward the surface eventually to emerge from springs.

1. Introduction

Accumulation and storage of water in sedimentary basins can provide favorable environments to form geothermal mineral resources (Craig, 1969; Lowenstein et al., 2003). Geothermal water is an environment-friendly resource, which can partially replace fossil fuels. Direct utilization of geothermal energy in a total of 82 countries is 592,638 TJ/year (164,635 GWh/year) at the end of 2014 (John and Tonya, 2016), preventing 149.1 million tonnes of CO_2 being released to the atmosphere. Geothermal water resources are widely used directly for heating, therapy and recreation and indirectly for power generation (Górecki et al., 2015; Sowiżdżał et al., 2019; Pang et al., 2018). The metallic and nonmetallic mineral resources in deep-seated subsurface brines are also widely used in salt making and industrial raw material supply (Lowenstein et al., 2003; Ryabtsev et al., 2020). As the development and utilization of middle-deep groundwater in evaporate basins can thus provide an important resource to help solve global resource and environmental issues, it is necessary to understand relevant formation mechanisms and the laws that govern distribution of these resources.

Worldwide, the hydrochemical characteristics of shallow circulating

* Corresponding author at: School of Geographical Sciences, Southwest University.
E-mail address: balance@swu.edu.cn (P. Yang).

https://doi.org/10.1016/j.jhydrol.2022.127782
Received 16 October 2021; Received in revised form 23 March 2022; Accepted 28 March 2022
Available online 31 March 2022

karst groundwaters, which are generally of a HCO_3-Ca or HCO_3-Ca·Mg type, are different from those of middle (0.3–2 km) and deep (>2 km) circulating water in karst systems (Hem, 1970). Shallow karst systems containing evaporites are easily leached, resulting in the loss of soluble salts. As the flow path becomes longer, the water flow can become almost stagnant which can result in the hydrochemical type gradually evolving into a SO_4-Ca and Cl-Na type with higher temperature and salinity (Ta et al., 2019; Chen et al., 2007). The hydrochemical characteristics of groundwater are controlled by geological structure and lithology. Permeability influenced by lithology exerts an important control on the rate of groundwater circulation, as variations in the hydrochemical type of groundwater can affect the extent of flushing of the rock strata (Schmoker and Halley, 1982). Several studies have emphasized the impact of geological structure on groundwater circulation (McIntosh and Ferguson, 2021; Dafny et al., 2010; Labat et al., 2021; Kong et al., 2020). The degree of structural development affects the evolution of hydrochemical types, and lithology provides the material basis for the formation of hydrochemical types. These two factors play different roles in different regions.

The total karst area in China is 344 × 10^4 km^2, accounting for >1/3 of the national area (Yuan et al., 2016). Chongqing is located in southwestern China (Fig. 1a), which has the most concentrated and contiguous karst area of karst landscape development. About 36% (3 × 10^4 km^2) of Chongqing is covered by karst. In Chongqing, lithology related to permeability is relatively consistent and can be used as the control variable. Tectonic topography then becomes the explanatory variable that controls the extent of water circulation, and in turn the hydrochemical type and water temperature. The Eastern Sichuan fold belt

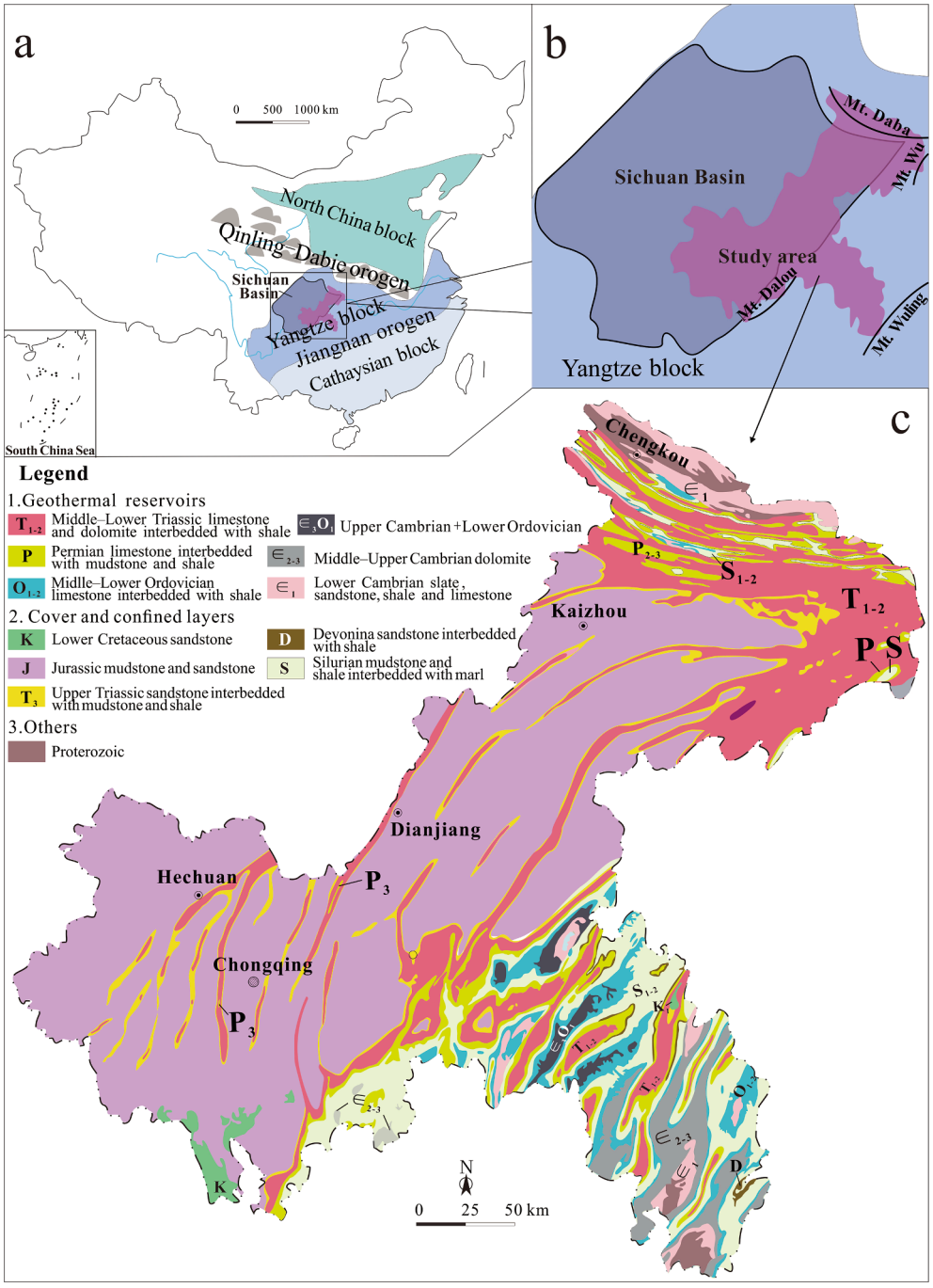

Fig. 1. (a) Location of Chongqing and an overview of the surrounding tectonic regions. (b) Topographic and structural diagram of Chongqing. (c) General geology of Chongqing (modified from Hu, 2017; Geological map of southwest China; Yan et al., 2018). The study area was mainly affected by the Qinling-Dabie and Jiangnan Orogens, with the tectonic stress transferred from NE to SW, and from SE to NW, respectively. The degree of stratigraphic weathering and denudation in the study area trends along the same direction, and the corresponding ages gradually became younger.

dominates the geologic structure of Chongqing, and is characterized by folds alternating between long, steeply dipping anticlines and wide gentle synclines. Within this belt, stratified thermal karst aquifers occur in uplifted mountain areas. Middle and Lower Triassic carbonate aquifers occur in the flanks of anticlines buried at depths of several hundred to >2,000 m (Wang et al., 2018; Yang et al., 2017), and these mainly host low-and medium temperature SO_4-Ca water. This is in contrast to shallow karst groundwater dominated by HCO_3^- and Ca^{2+} (Pu et al., 2010), but typical for mid- to deep carbonate waters. Previous geothermal resource development, utilization and research have mainly been concentrated in the Eastern Sichuan fold belt, while only a handful of studies have focused on other local areas of consistent internal geological structure in Chongqing (Cheng et al., 2015; Cao, 2014; Guo, 2019; Luo et al., 2019; Ta et al., 2018, 2019; Xiao, 2012; Yang et al., 2017, 2019; Zeng, 2012). In the higher level of geological tectonic divisions, all of Chongqing belongs to the Middle-Upper Yangtze Block. The internal subregions of Chongqing are interrelated with each other, so that the distribution, formation and evolution mechanisms of middle-deep groundwater in the different regions are relatively homogeneous. Details of the flow paths and even the recharge areas are poorly characterized, both of which are obviously of great importance in the exploration of geothermal water and brines.

In this context, this paper studies the whole of Chongqing at the level of the Middle-Upper Yangtze Block. The goals of this paper are to explore the origins of middle-deep groundwater, water-rock interactions, and runoff processes. Finally, the geological temporal evolution and spatial distribution of the openness degree of middle-deep groundwater systems in Chongqing under the influence of geological structure are clarified, providing reference for the exploration, comprehensive exploitation and sustainable utilization of geothermal resources.

2. Study area

2.1. Geographical setting

Southwest China's Chongqing Municipality is located between N 28°10′–32°13′ and E 105°17′–110°11′, covering an area of 8.24×10^4 km^2. There were 142 thermal water access points (warm springs and drilled warm springs) by the end of 2014, thus it has been called "the hot springs capital of China".

The landscape in Chongqing consists mainly of hills and mountains, and it is known as a mountain city (Wang et al., 2018). The north, east and south are surrounded by Mt. Daba, Mt. Wuling and Mt. Dalou, respectively (Fig. 1b). The area is characterized by a subtropical humid monsoon climate with mean annual air temperature and rainfall from 17 to 23 °C and >1000 mm, respectively. The wet season is from May to September, accounting for about 53% of the total annual precipitation. The dry season occurs in December and January to March of the following year (Yang et al., 2019).

2.2. Geological settings

Geological formations from Upper Sinian to Middle Triassic in the study area are mainly marine carbonates interbedded with clastic rocks and evaporates (gypsum and/or anhydrite and halite) (Fig. 1c). They have undergone multicyclic tectonic movement, varying in a thickness from ~ 4 to 7 km. The underlying Lower Paleozoic marine black mud shale has high hydrocarbon generation potential (Guo, 2015). The strata from the Upper Triassic to the Cretaceous are red sandstone and mudstone deposits of lacustrine facies, ranging in a thickness from ~ 2 to 6 km (Mou et al., 2014; Luo and He, 2014; Zhou et al., 1997).

According to finer tectonic subdivisions, Chongqing is divided into the Central Sichuan gentle fold belt located to the west of the Mt. Huaying basement fault, the Eastern Sichuan fold belt located to the west of the Mt. Qiyao basement fault, the Qianyuxiange uplift fold belt located to the east of the Mt. Qiyao basement fault, and the Mt. Daba arc-like fault fold belt located to the north of the Shashi hidden fault (Fig. 2). Different hydrogeological conditions are the key factors affecting hydrochemical composition of groundwater (Drogue et al., 2000). Therefore, the study area can be divided into three divisions according to the different tectonic units and outcrops (Fig. 2):

2.2.1. Midwest Chongqing (MWC)

The Central Sichuan Anteklise is located in the westernmost part of Chongqing and, of the Mt. Huaying basement fault. Because its geological structure is similar to the syncline of the Eastern Sichuan fold belt, it is classified into this category. There are mostly NE-to NNE-trending, short-axis gently dipping anticlines in the Central Sichuan Anteklise, and the strata dip angle is generally 1–3° (Li et al., 1980). Jurassic red sandstone and mudstone are the main outcropping formations (Luo, 1987). Faults are rare and the structures and lithology are simple, so the soluble salts of protogenetic deposits in the strata can be preserved (Li et al., 1977). The Eastern Sichuan fold belt is characterized by a succession of nearly parallel NNE-trending, narrow, asymmetric steeply dipping anticlines and nearly symmetrical broad gentle synclines. The elevation of the low ranges formed by these anticlines is generally between 500 and 900 m, and the synclines form relatively broad hills ranging in elevation from 300 to 500 m (Chen, 1977). The faults of the wide and gentle synclines are not developed, but the deep-seated faults of the Triassic Jialingjiang Formation and the older strata near the axis of the high uplift anticline are well developed (Luo, 1987; Tan, 1990; Wang and Zhang, 2004). These are mainly small-scale compression-torsional thrust faults that have become pathways for deep-formation thermal fluids. Middle and Lower Triassic marine sedimentary rocks occur at the axis of the anticlines, varying in a thickness from 600 to 1000 m, and are the main reservoirs of middle-deep groundwater (Yang et al., 2007). The Upper Triassic Xujiahe Formation, which has poor thermal and water conductivity and serves as a cap rock, is composed of feldspar-quartz sandstone imbedded with carbonaceous shale and coal seams with a thickness of about 400 m, mainly outcropping in the flanks and cores of anticlines. The Lower Triassic Feixianguan (or Daye) Formation is argillaceous rock interbedded with limestone with a thickness of ~ 500 m and exhibits low permeability and thermal conductivity (Cheng et al., 2015).

2.2.2. Southeast Chongqing (SEC)

Southeast Chongqing is located to the southeast of the Mt. Qiyao basement fault, and the Paleozoic strata are widely distributed. It is characterized by a series of NE-trending synclines and anticlines, cut by faults. From NW to SE, the folds change from narrow anticlines and wide synclines to wide anticlines and narrow synclines, and the intensity of structural deformation gradually strengthens as the outcrops gradually evolve through time (Hu, 2017). Most folds form low-to-medium-sized mountains ranging in elevation from 1000 to 1300 m. Normal faults are well developed, mostly occurring in the axes of anticlines, and are the main pathways for the ascent of middle-deep groundwater. The Devonian and Silurian strata serve as aquitards with a thickness of nearly two kilometers, located in the anticlinal flanks, sandwiched between the Cambrian and Ordovician carbonate aquifers. These mainly outcrop in anticlines while the Permian and Triassic carbonate aquifers mainly outcrop in synclines (Zhou et al., 2017). There are more halite pseudocrystal and gypsum layers in the middle Cambrian section. The total thickness of sedimentary the strata is ~ 7700 m, and the Lower Paleozoic marine carbonate strata are the most well-developed and widely distributed with a thickness of ~ 4545 m (Xia et al., 1979).

2.2.3. Northeast Chongqing (NEC)

The Northeast Chongqing section includes the Shashi hidden fault, the Mt. Daba arc-like fault fold belt to the north, and the area to the east of the Mt. Qiyao basement fault in northeast Chongqing. The latter is adjacent to the Mt. Daba arc-like fault fold belt which is structurally

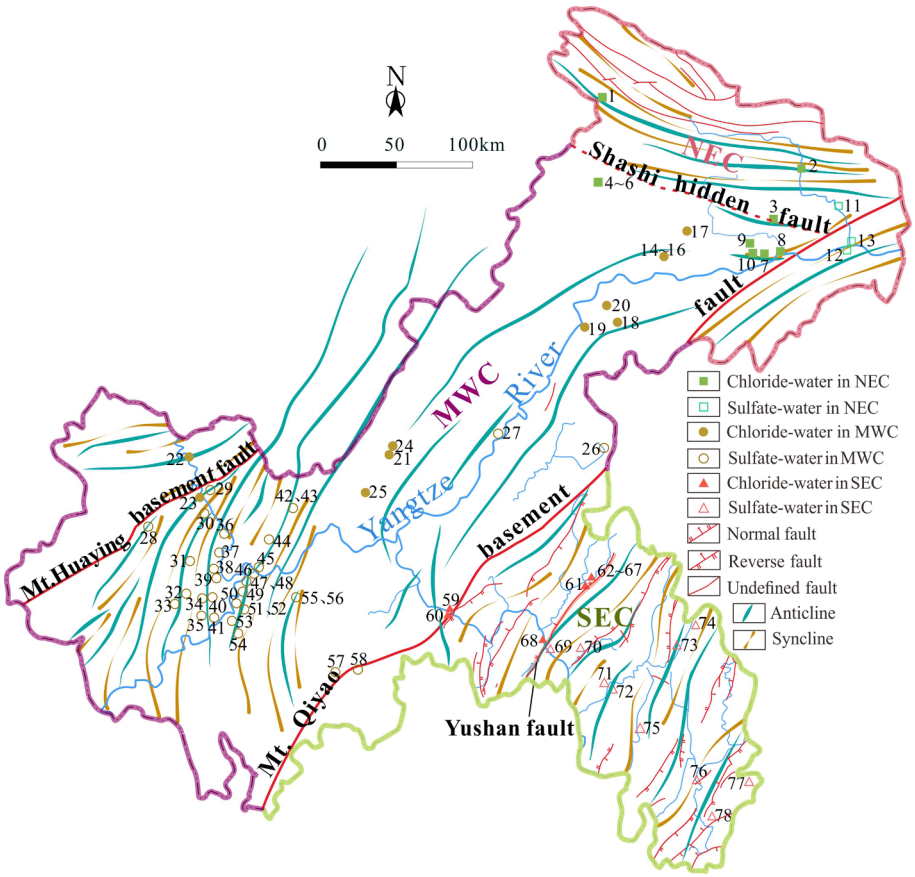

Fig. 2. Generalized structure of the study area with sampling locations (modified from Zhang et al., 2015; Hu, 2017). The study area is divided into three parts, including Midwest Chongqing (MWC), Southeast Chongqing (SEC) and Northeast Chongqing (NEC). The internal structure of the three subareas is relatively uniform, and bounded by the Mt. Qiyao basement fault and the Shashi hidden fault.

similar, and the outcrops are all mostly Middle and Lower Triassic, so they belong to the same area for discussion. There are mainly a series of NW-trending and SW-protruding arc-shaped faulted folds, accompanied by high angle thrust faults and strong compression. The density of folds and faults weakens towards the southwest (Lin, 2016) as the altitude decreases from 2200 to about 1500 m (Chen, 1977). The rock formations have steep dip angles and provide the thermal fluid migration channels. The outcrops include a large area of carbonate rock and a small amount of interbedded, insoluble rock ranging from Upper Sinian to Lower Triassic. The Lower Triassic strata are the most widely distributed, mostly occurring in the cores of synclines. The Lower Cambrian strata mostly occur in the cores of anticlines. Ordovician and Permian strata constitute the main potential thermal reservoirs, and the Lower Triassic Daye Formation forms a cap rock. Lower Permian, Devonian and Carboniferous formations serve as aquitards. The Lower Triassic Jialingjiang Formation constitutes the secondary potential thermal reservoir, with a cap rock formed by the Middle Triassic Badong formation.

3. Methodology

3.1. Sampling and measurements

This paper summarizes strata lithology and the evolutionary history of geological structure based on previous literature and geological maps. Physicochemical data of the middle-deep groundwater in Chongqing and the data related to the exploitation of geothermal wells were collected and combined with the data of 19 thermal waters in SEC obtained during November 2017 and July 2018. Field sampling methods, laboratory tests and corresponding data have been reported in literature (Yang et al., 2019b). The data of the remaining 59 water samples are from Yang et al. (2017), Guo (2019), Luo et al. (1981), Gong (2016) and Zhou et al. (1980). All of the sample locations are shown in Fig. 2. The temperature, pH, major ions, total dissolved solids (TDS) and hydrogen and oxygen isotopes (if any) were compiled. The aforementioned data and their extreme values, mean values, standard deviation and corresponding calculation results are shown in Table A.1. All values are expressed as mean ± one standard deviation.

3.2. Data processing

3.2.1. Saturation index (SI)

The Saturation Index (SI) was calculated using PHREEQC version 3 (Parkhurst and Appelo, 2013). When SI <0, the solution is undersaturated. When SI = 0, mineral dissolution and precipitation reach equilibrium and the solution is saturated. When SI >0, the solution is oversaturated and minerals are predicted to precipitate.

3.2.2. Geothermometers

There are reaction equilibrium relationships between mineral solubility and temperature, with which a series of empirical formulas can be established to estimate reservoir temperature (Arnorsson, 1985), and these are called geothermometers. Silica geothermometers and cation geothermometers are widely used. The calculations used in this study are as follows:

(1) Quartz (Fournier, 1977), $T_1 = [1309/(5.19 - \lg SiO_2)] - 273.15$.

(2) Improved SiO_2 (Verma and Santoyo, 1997), $T_2 = -44.119 + 0.24469SiO_2 - 1.7414 \times 10^{-4}SiO_2^2 + 79.305\lg SiO_2$.

(3) K-Mg (Giggenbach, 1988), $T_{K\text{-}Mg} = 4410/[14 - \lg(K^2/Mg)] - 273.15$.

(4) Na-K-Ca (Fournier and Truesdell, 1973), $T_{Na\text{-}K\text{-}Ca} = 1647/[\lg(Na/$

K) + βlg(√Ca/Na) + 2.24] – 273.15.

The coefficient β of formula 4 is 4/3 for calculated temperatures below 100 °C and 1/3 for calculated temperatures above 100 °C (Fournier and Truesdell, 1973), where, T is the estimated reservoir temperature in °C; SiO_2, Na, K, Ca and Mg are their corresponding concentrations in mg/L.

3.2.3. Circulation depth

The circulation depth is calculated by Eq. (1) (Lin, 1993):

$$Z = (T_z - T_0)/G + Z_0 \quad (1)$$

where Z is the circulation depth in km; T_z is the estimated reservoir temperature in °C; The local mean annual air temperature (T_0) is set to 18 °C in NEC and MWC, and 16.5 °C in SEC (https://www.tianqi.com/); The geothermal gradient (G) is assumed to be 30 °C/km for MWC (Xu et al., 2011), 17 °C/km for NEC (Fan et al., 2014), and 21 °C/km for SEC (Luo et al., 2019). Z_0 is the depth of the constant temperature zone in km, which in Chongqing is about 80–100 m (Zhou et al., 2017), thus taking the average depth of 0.09 km as the value of Z_0.

4. Results

4.1. Hydrogeochemistry

Piper plots can intuitively show water samples of different hydrochemical facies according to the proportions of major ions (Chadha, 1999). Considering the TDS values, the water samples can be roughly classified into two hydrochemical categories: Sulfate-water dominated by Ca^{2+} and SO_4^{2-} and lower TDS values ranging 1000–3000 mg/L and chloride-water dominated by $Na^+$and Cl^- and higher TDS values >5000 mg/L (Fig. 3).

Among chloride-waters, average TDS values in MWC, NEC and SEC decrease successively, which are 146580 ± 120144, 57641 ± 88694 and 16048 ± 11534 mg/L, respectively (Fig. 3). The average discharging temperatures in MWC, SEC and NEC are 40.8 ± 9.5, 31.6 ± 14.3 and 25.4 ± 8.2 °C, respectively (Table A.1).

Among sulfate-waters, the average discharging temperatures and TDS values in NEC (19.8 ± 1 °C, 731 ± 82 mg/L) are lower than those in MWC (45.2 ± 7.9 °C, 2484 ± 786.6 mg/L). The average discharging temperatures and TDS values of SEC are 41.5 ± 6.5 °C and 1020.3 ± 770.5 mg/L, respectively, which are between those of MWC and NEC (Table A.1).

4.2. Saturation index (SI) and hydrochemical balance

The SIs of quartz in middle-deep groundwater range from 0.2 to 1.1, and these imply oversaturation but close to saturation (Table 1). The SIs of halite are <0 implying undersaturation. The SIs of anhydrite, calcite, dolomite and gypsum range over positive and negative values, which indicate the dissolved minerals vary between oversaturation and undersaturation.

The Na-K-Mg triangular plot proposed by Giggenbach (1988) can be used to identify the water–rock equilibrium, and categorize groundwater into three groups: fully equilibrated water, immature water that has been mixed with shallow water during deep-seated thermal fluid ascent and/or re-equilibrates along the circulation flow path, and partially equilibrated water in between. Sulfate-waters in SEC and MWC are at the Mg^{2+} corner and showing immature water (Fig. 4), suggesting that the groundwater has been mixed with shallow, cold groundwater in the ascending process. Chloride-water data points are mostly located in partially equilibrated and mature water zones.

4.3. Reservoir temperature and circulation depth

The geothermometer is based on temperature-dependent water–rock chemical equilibrium, so the mineral equilibrium of water samples should be tested first (Giggenbach, 1988). Fig. 4 shows that part of the chloride-waters are in the full equilibrium area, so the cation geothermometer is available. The Na-K geothermometer is applicable to high-temperature (>180 °C) geothermal systems (Arnorsson, 1985). The δD and $\delta^{18}O$ of groundwater show no significant positive $\delta^{18}O$ shift (Fig. 5), indicating that the maximum reservoir temperature is below 100 °C (Mayo and Loucks, 1995), thus the Na-K geothermometer is not applicable. The K-Mg geothermometer is suitable for low-temperature geothermal systems (Giggenbach, 1988). The Na-K-Ca geothermometer is suitable for geothermal water that is rich in calcium (Fournier and Potter, 1995). Quartz dissolved in groundwater is generally oversaturated (Table 1), thus the quartz geothermometer (Fournier, 1977) and the improved SiO_2 geothermometer (Verma and Santoyo, 1997) are suitable for the calculation of reservoir temperature, resulting in a value of >70 °C. The calculation results of reservoir temperatures are shown in Table A.1.

Compared with the discharging temperatures, the reservoir temperatures calculated by the K-Mg geothermometer are lower in the sulfate-waters of MWC and SEC, and others are higher. The Na-K-Ca geothermometer is suitable for calcium-rich geothermal water, so it is not feasible to calculate the reservoir temperatures for chloride-water

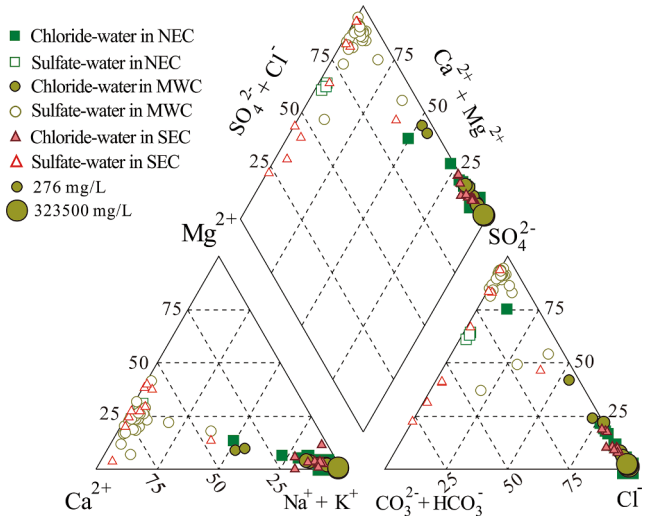

Fig. 3. Piper plot of the middle-deep groundwater samples.

Table 1
Calculated SIs of middle-deep groundwater samples. – denotes no data.

Zone	Anhydrite	Calcite	Dolomite	Gypsum	Halite	Quartz
Chloride-water in NEC	–1.3–0.3	0–2.9	–0.4–5.8	–1.2–0.2	–6.1–0.1	0.4–0.7
Sulfate-water in NEC	–1.2 - –1	0.1	–0.1	–0.9 - –0.8	–8.7 - –8.4	–
Chloride-water in MWC	–0.7–1.5	0.1–2.3	–0.1–4.4	–0.6–1.3	–4.6–1.1	0.2–0.6
Sulfate-water in MWC	–1.7–0	–0.2–1.6	–1.2–2.9	–1.5–0.03	–9.4 - –6.5	0.3–0.5
Chloride-water in SEC	–1.7 - –0.5	–0.6–0.8	–1.8–1	–1.5 - –0.2	–4.6 - –2.3	0.2–0.9
Sulfate-water in SEC	–2.2 - –0.3	–0.4–0.7	–2.1–1.3	–1.9 - –0.1	–11.1 - –5.9	0.5–1.1

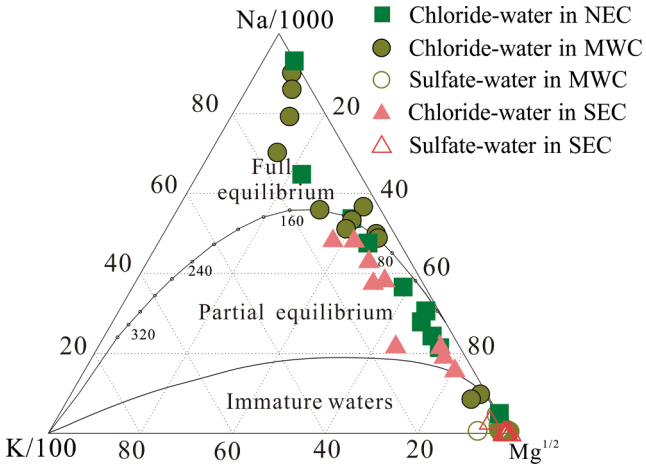

Fig. 4. Na-K-Mg Giggenbach plot of the middle-deep groundwater samples.

dominated by Na^+ and Cl^-, and the calculated temperatures of sulfate-water are lower than discharging temperatures. The results of quartz geothermometer and the improved SiO_2 geothermometer are slightly higher than the groundwater outflow temperatures (Table A.1), which proves that the calculation results are reasonable. In summary, taking the average value of the calculation results of quartz geothermometer and the improved SiO_2 geothermometer, the estimated reservoir temperatures of sulfate-water in SEC and MWC are the highest, averaging at 82 ± 15 and 78 ± 9 °C, respectively. The estimated reservoir temperatures of chloride-water in MWC are slightly higher than that in SEC, averaging at 69 ± 8 and 64 ± 18 °C, respectively. The estimated reservoir temperatures of chloride-water in NEC are the lowest, averaging at 55 ± 27 °C. These values are consistent with the temperature range (64–104 °C) of geothermal reservoir data obtained from the Chongqing Geological Survey (Chongqing Municipal People's Government, 2010).

Groundwater temperature depends on circulation depth, geothermal gradient, exothermic reactions in water–rock interactions, magmatic activity and active faulting (Yang et al., 2017). To the east of the Mt. Huaying basement fault in the study area is the basement area of weak-to-non-magnetic and low-grade metamorphic rocks of Mid-Late Proterozoic, without an active magmatic heat source and radioactive heat

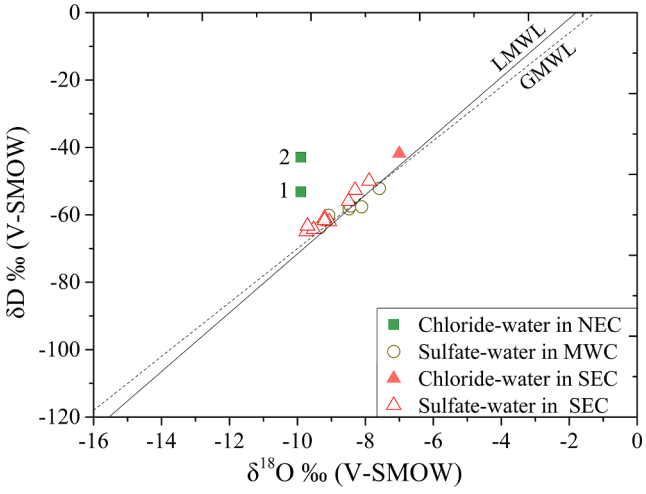

Fig. 5. δD vs. $\delta^{18}O$ of middle-deep groundwater samples. Except for samples 1 and 2 of NEC, the rest of the water samples fall near the CMWL (Li et al., 2010) and the GMWL (Craig, 1961), suggesting that the middle-deep groundwaters originated from precipitation. The positive δD of nos. 1 and 2 may be due to bacterial sulfate reduction or thermal-chemical sulfate reduction reactions.

generation (Fig. 2). To the west of this fault is the basement area of Archean, strongly magnetic and medium-basic igneous rocks (Luo, 1987; Feng et al., 2019). We can conclude that waters examined in this research are mainly heated by terrestrial heat, as such the circulation depth can be estimated via the geothermal gradient and reservoir temperature as expressed by Eq. (1). The average maximum circulation depths of sulfate-water in SEC and MWC are 3.2 ± 0.7 and 2.1 ± 0.3 km, and that of chloride-water are 2.3 ± 0.8 and 1.8 ± 0.3 km, respectively. The average maximum circulation depths of chloride-water in NEC are 1.3 ± 0.9 km (Table A.1), which are the shallowest among the three regions. Comparing the calculated results of 31 geothermal drilling water samples with the well depths (Table A.1), it was found that the calculated circulation depth of 5 water samples is slightly less than the geothermal well depth, and the relative error range is 0.7%–5.8%. This may be due to the mixing of middle-deep groundwater with shallow groundwater, resulting in the calculated circulation depth being less than the actual circulation depth shown by the geothermal wells, but the error is within a reasonable range. The exploration results of >30 drilled wells in MWC demonstrate that most well waters are in the 2nd through the 4th members of the Jialingjiang Formation with depth of about two kilometers. The 1st member and older strata (depth >2.5 km) have low porosity and poor water abundance (Yang et al., 2007).

5. Discussion

5.1. Origin of the middle-deep groundwaters

Oxygen and hydrogen isotopes are relatively stable in groundwater circulation and can be used as tracers to determine the potential origin of groundwater and water–rock interactions (Craig, 1961). Hydrogen and oxygen isotope studies have shown that thermal springs with a low enthalpy background are most likely replenished by rainfall (Soraya et al., 2019). The current study area mostly belongs to a low enthalpy thermal water area (Wang et al., 2018). Fig. 5 shows that $\delta^{18}O$ and δD values of all the data points (n = 19) except numbers 1 and 2 fall near the Chongqing Meteoric Water Line (CMWL; Li et al., 2010) and the Global Meteoric Water Line (GMWL; Craig, 1961), indicating that the middle-deep groundwaters originated as meteoric water. This is in agreement with the conclusions drawn by Luo et al. (2006) and Yang et al. (2019) that the recharge of thermal waters in the SEC and the southern part of MWC originated from precipitation in the late Pleistocene.

5.2. Principal geochemical processes

The chemical composition of middle-deep groundwater is the result of water–rock interaction under high temperature conditions, governed by the chemical composition of country rock minerals (Huang et al., 2019). The key mineral components of the carbonate-evaporite rocks (e.g., the Lower Triassic Jialingjiang Formation) are calcite and dolomite, followed by secondary minerals such as anhydrite, pyrite, halite, quartz and celestite, which provide a material basis for the chemical composition of geothermal water (Han, 2002). It can thus be assumed that based on geological structure and lithology analyses combined with hydrochemical characteristics, the origin of groundwater, principal geochemical reactions and the evolution of chemical composition can be determined (Christina et al., 2014; Zarei et al., 2013).

When the equivalent ratio of $(Ca^{2+} + Mg^{2+})$ / $(HCO_3^- + SO_4^{2-})$ is 1:1, the ions are controlled by the solubility equilibrium of carbonate and gypsum (Guo et al., 2018; Marghade et al., 2020). Most of the data points in Fig. 6a are close to the 1:1 line, indicating that the equilibrium dissolution of gypsum (and/or anhydrite) and carbonate minerals are the main source of Ca^{2+}, Mg^{2+}, HCO_3^- and SO_4^{2-} in the water.

When carbonate rock dissolution is dominant, the meq/L ratio of $(Ca^{2+} + Mg^{2+})$ / HCO_3^- is 1:1, and the Ca^{2+}/SO_4^{2-} equivalent ratio of gypsum dissolution is 1:1 (Choi et al., 2012). $(Ca^{2+} + Mg^{2+})$ /HCO_3^- equivalent ratios for most data points deviate far away from 1:1 line (Fig. 6b), and the Ca^{2+}/SO_4^{2-} equivalent ratios mostly fall near the 1:1 line (Fig. 6c), indicating that Ca^{2+} and SO_4^{2-} in waters are mainly from gypsum and /or anhydrite dissolution in equilibrium. The Ca^{2+}/SO_4^{2-} equivalent ratios of some chloride-waters (including sample no. 1) in NEC and MWC show a nonlinear relationship (Fig. 6a, c), which may be due to bacterial sulfate reduction (Christina et al., 2014; Drogue et al., 2000) or thermal-chemical sulfate reduction reactions (Machel et al., 1995; Krouse and Viau, 1988) involving water and hydrocarbons under high temperature and pressure reducing conditions. The reaction reduces SO_4^{2-} to H_2S gas and consumes light isotopes first, making the δD of

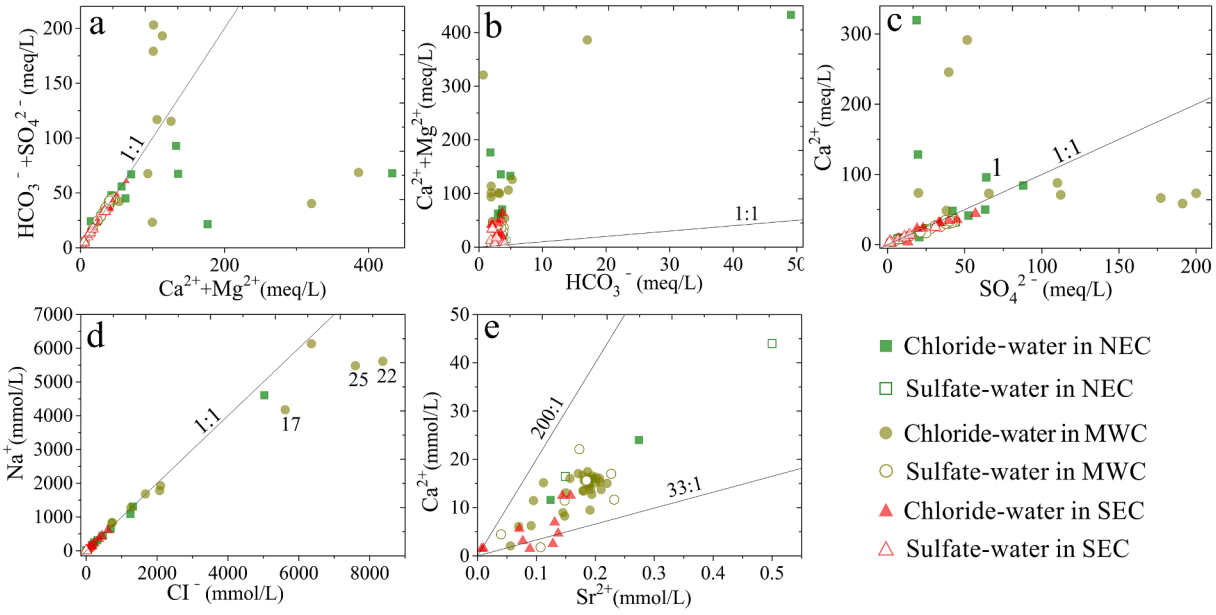

Fig. 6. Ratios of ions in the middle-deep groundwater within the study area, including (a) $(HCO_3^-+SO_4^{2-})/(Ca^{2+}+Mg^{2+})$, (b) $(Ca^{2+}+Mg^{2+})/HCO_3^-$, (c) Ca^{2+}/SO_4^{2-}, (d) Na^+/Cl^-, (e) Ca^{2+}/Sr^{2+}.

water sample number 1 formed by rainfall dissolving halite more positive (Fig. 5). In Fig. 6d, the molar ratios of Na^+/Cl^- mostly fall near the 1:1 line, indicating that they are from the dissolution of halite formations. Water-rock interactions can release heat. At 18 °C, the heat released during anhydrite dissolution is 4.44 kcal/mol (Gao et al., 2008), thus the dissolution of sulfate rocks and halite can heat middle-deep groundwater.

Sr^{2+} exists in the crystal lattice of gypsum, and has leached into groundwater with gypsum. The precipitation of $SrSO_4$ is later than that of $CaCO_3$, and earlier than that of $CaSO_4{\cdot}2H_2O$ and $CaSO_4$ (Shen, 2010). Therefore, Sr^{2+} is not enriched in the carbonate deposits, and the content of Sr^{2+} in groundwater from the carbonate reservoir is low. Thus, the molar ratio of Ca^{2+}/Sr^{2+} is high, close to 200. In marine, connate sedimentary waters, the ratio of Ca/Sr is generally about 33 (Guo, 2019). The TDS values of sample numbers 72 and 73 of SEC are as low as 396.26 and 276 mg/L, and the molar ratios of Ca/Sr are close to 200, that is, 152 and 194, respectively (Fig. 6e), indicating that these may have come from carbonate formations without gypsum, resulting in low Sr^{2+} and salinity. The molar ratios of Ca/Sr in the remaining data points are mostly between 33 and 200, and this is likely due to the dissolution of sulfate formations.

In the dissolution processes of the minerals above, the water–rock interaction dissolves the reservoir, which provides ideal channels for groundwater transport in the middle and deep strata.

5.3. Evolution of hydrochemical types in geological history

Under favorable structural conditions, evaporated seawater can be trapped in marine carbonate rocks. In study area, marine sedimentary metamorphic black brine mainly occurs in the Middle and Lower Triassic carbonate aquifers in confined, low-gentle anticlines with low tectonic pressures (Cao, 2014; Chen et al., 2014; Lin and Pan, 2001; Zhou et al., 2018). The black brine has a black sediment of turbid suspended solids, strong hydrogen sulfide odor and high heavy metal content. It originated as a mixture of gypsum crystal water dissolving halite and residual paleo-evaporated seawater (Lin, 2006; Wang, 1989; Zhou et al., 1997). The strata and structures where the brine is located are also where some of the middle-deep circulating groundwater is located, such as the Hechuan Dashiqiao anticline (No. 22), the Dianjiang Wolonghe anticline (Nos. 21 and 24), the Kaizhou Wenquan anticline (Nos. 4–6) and the Yunanchang anticline (Nos. 14–17) (Gong, 2016). The deep formation brine can become the replenishment source of middle-deep groundwater during structural evolution. The mixing of brine and meteoric water can increase the concentration of Cl^-, Na^+ as well as Br^-, a characteristic element in marine sedimentary brines, in the middle-deep groundwater (Richard et al., 2011). Na/Cl and $Br \times 10^3/Cl$ coefficients are the coefficients with greatest stability in seawater, which can be used to determine the origin of groundwater (Fig. 7). The molar ratio of Na/Cl in standard seawater ranges from 0.85 to 0.87. When seawater evaporates and becomes concentrated to the point of halite deposition, the molar ratio of Na/Cl decreases continuously, so the ratio of depositional metamorphic brine is generally < 0.87 and that of non-marine leaching brines is generally greater than or close to 1 (Stiller et al., 2009; Vengosh et al., 2002). When dissolved salts begin to deposit with the evaporation of lake water in enclosed lake basins, less soluble carbonates ($CaCO_3$, $CaMg(CO_3)_2$) are deposited first, followed by sulphates ($CaSO_4$, Na_2SO_4, $MgSO_4$), and chlorides (NaCl, $KMgCl_3$) last (Shen, 2010). Thus, the molar ratio of Na/Cl can also decrease, sometimes even below 0.87, when dissolving the strata containing chlorides of the last deposition stage (Stiller et al., 2009).

Br^- takes a minimal part in the reactions that form solid minerals in the process of evaporation and concentration of seawater. Only a small fraction of bromine ions replace chloride ions in the form of isomorphism into solid salts, and most Br^- remains in the residual evaporated seawater. The Br^- content of residual evaporated seawater increases linearly with evaporation and concentration. The $Br \times 10^3/Cl$ molar ratio of modern seawater is 1.5 (Fontes and Matray, 1993). Halite precipitation consumes 1:1 mol of Na^+ and Cl^-, thus the $Br \times 10^3/Cl$ molar ratio of residual evaporated seawater is >1.5 (the seawater value). The $Br \times 10^3/Cl$ molar ratio of sedimentary halite is between 0.05 and 0.3. Correspondingly, that ratio of dissolved-halite precipitation is <0.3. When potassium halide is deposited, the $Br \times 10^3/Cl$ molar ratio in the residual evaporated seawater increases to 25, and the sylvite deposited at the same time is also rich in Br^-. Therefore, that ratio of rainwater dissolving potassium and magnesium salts is >1 (Hao et al., 2020; Vengosh et al., 2002). Samples numbers 17, 22, 23, 24 (Fig. 7) and 25 (Fig. 6d) in MWC are not stagnant sedimentary metamorphic brine, and their Na/Cl molar ratios range from 0.476 to 0.845. The data suggest that these water samples probably originated from rainwater-leached potassium and magnesium salts or rainwater mixed with sedimentary metamorphic brine (Fig. 7). These water samples are in the transition stage of the dynamic process of marine sedimentary metamorphic brine being replaced by rainwater. With the progress of weathering and denudation, middle-deep groundwater undergoes part or all of this process: marine sedimentary metamorphic brine → flushing out of brines by meteoric water → rainwater principally dissolves chloride

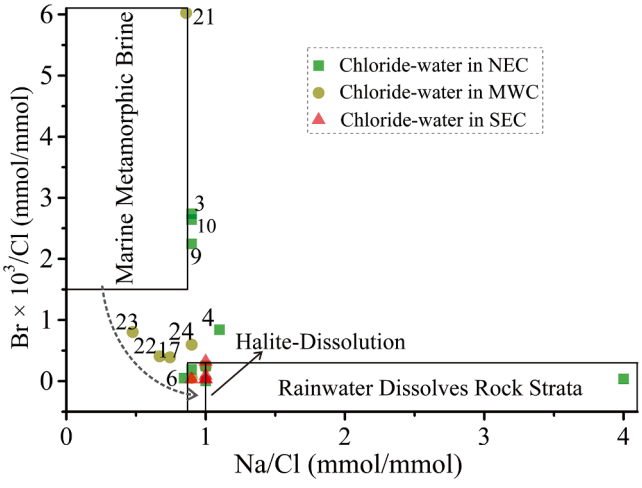

Fig. 7. Molar ratios of $Br \times 10^3/Cl$ and Na/Cl of chloride-water. The Br^- values of sample numbers 4, 14, 15, 16, 61, 63, 64 and 67 were missing; Br^- values of sample numbers 20, 25 and 60 could not be detected.

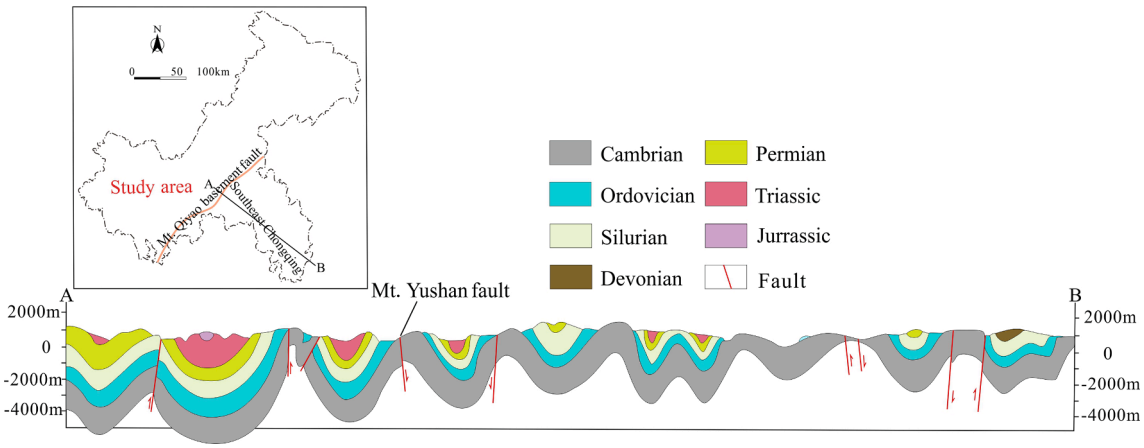

Fig. 8. Geologic cross-section of A-B in SEC (modified from Hu, 2017).

minerals → rainwater principally dissolves sulfate minerals → rainwater principally dissolves carbonate minerals. The hydrogeological cycle of the study area starts from the continental clastic rocks deposited in the upper Triassic, and now enters the second stage of the cycle, that is, the denudation leaching period. The middle-deep groundwater system is still in the dynamic process of residual metamorphic paleo-seawater of the previous hydrogeological cycle diluted in places by rainwater.

5.4. Geologic tectonic process and distribution of hydrochemical type

The middle-deep groundwaters in SEC mainly occur in the Cambrian, Ordovician and Permian formations. To the west of the Yushan fault chloride water occurs, with sulfate water to the east (Fig. 2) (Yang et al., 2019b). From the axes to the flanks of steeply dipping anticlines in MWC, on which karst valleys develop, the hydrochemical types of groundwater in the Middle and Lower Triassic formations change from the bicarbonate type to the sulfate type, and chloride-water mostly occurs in synclines and confined anticlines. In NEC, sulfate-water mainly exists in synclines within the large area of Triassic carbonate outcrops, and chloride-water mainly occurs in the Paleozoic formations of the secondary anticline and the tectonically confined Triassic strata (Chen, 1977; Luo et al., 1981) (Figs. 1, 2).

Different hydrochemical types may be primarily related to two factors. One is lithology, the other is the strength of tectonism. The formation of most of the giant halite and sulfate sedimentary layers in the strata is related to the evaporation and precipitation after seawater percolates into enclosed depressions (Warren, 2010). Marine evaporites in the study area are widely distributed. There are three salt-forming ages in the study area: Sinian, Cambrian and Early-Middle Triassic (Ma et al., 1988; Lin, 1999). The tectonic framework of the study area was formed during the Indosinian-Yanshan epoch. Indosinian was a period of amalgamation of the main plates in China. During this period, The Cathaysian Block and the Yangtze Block were the first to complete the amalgamation at the end of Middle Triassic, and the Qinling-Dabie Orogenic Belt was formed in the Late Triassic. The mountains formed during this period have been flattened. The Sichuan Basin was formed in the Yanshanian (Jurassic to Early Cretaceous), and the current mountain range was formed later. However, the distribution of hydrochemical types in this area is very consistent with the current geological structure and topography. Therefore, under the background of widespread distribution of evaporites (including salt rock) in Cambrian and Early-Middle Triassic, it can be inferred that different groundwater circulation velocities and recharge conditions controlled by tectonic movement are the primary reason for such distribution of hydrochemical types, which is of great significance for the preservation of soluble components (Coomar et al., 2019).

Chongqing is located in the Middle-Upper Yangtze Block (Fig. 1a). The Jiangnan Orogenic Belt has formed from the collision and extrusion of the Yangtze Block and the Cathaysian Block forms a tectonic stress transmitted from SE to NW in Chongqing. Chengkou and the area to the north of it belong to the Qinling geosynclinal fold system (Fig. 1; Wang et al., 2018). Under the action of the Qinling-Dabie Orogenic Belt formed by the collision of the Yangtze Block and the North China Block, the tectonic stress of the shallow crust was transferred from NE to SW, and strong extrusion resulted in the the Mt. Daba arc-like fault fold belt projecting to the SW (Fig. 1b; Wang et al., 2017; Yan et al., 2018). The whole tectonic framework was generated in the Indosinian and Yanshanian movements, and the previous tectonic framework was transformed in different degrees by the Himalayan movement (Wang et al., 2018). From SEC and NEC to MWC, the deformation time was delayed progressively, and the degree of compression deformation decreased, which has resulted in the corresponding changes of the properties related to the degree of tectonic opening and topographic gradients of circulation depth, water temperature, influence of meteoric water and TDS. The strata in SEC and NEC are broken and have open hydrological connectivity. The central and eastern part of MWC has medium hydrological connectivity, with both closed and open strata. To the west of the Mt. Huaying basement fault, its hydrological connectivity is poor and the strata are closed. (Fig. 2).

In SEC, heat and water conduction by faults are assumed to be major controlling factors of middle-deep groundwater channels (Yang et al., 2019). From SE to NW, there is a gradual variation from trough-like folds with wide anticlines and narrow synclines to partition style folds with narrow anticlines and wide synclines (Fig. 8). The fold strength and the degree of aquifer filtration and dilution decreases along the same gradient, resulting in the change of sulfate-water to chloride-water, and average maximum circulation depths also decreases from 3.2 ± 0.7 to 2.3 ± 0.8 km (Table A.1).

In NEC, large areas of Triassic carbonate rocks that contain salts, where halite and sylvite occur in synclines (Lin, 1999), constitute the most enriched strata of underground formation water (brine) in the Sichuan Basin (Zhou et al., 2014). The anticlines are Paleozoic salt-bearing strata, including those from the Cambrian, Ordovician and Permian, all of which are favorable for the formation of chloride-water under suitable structural conditions. Although the folding and denudation are intense in SEC and NEC, the ancient Paleozoic strata have been exposed relatively recently. The evaporites in the strata that have not been excessively dissolved and filtered can still form saline springs.

In MWC, thick Jurassic sandy mudstone caprocks are distributed in synclines and low gentle anticlines, within which the relatively weak tectonic stresses and the good sealing capacity greatly weaken the intensity of water circulation and preserve the soluble salts of protogenetic

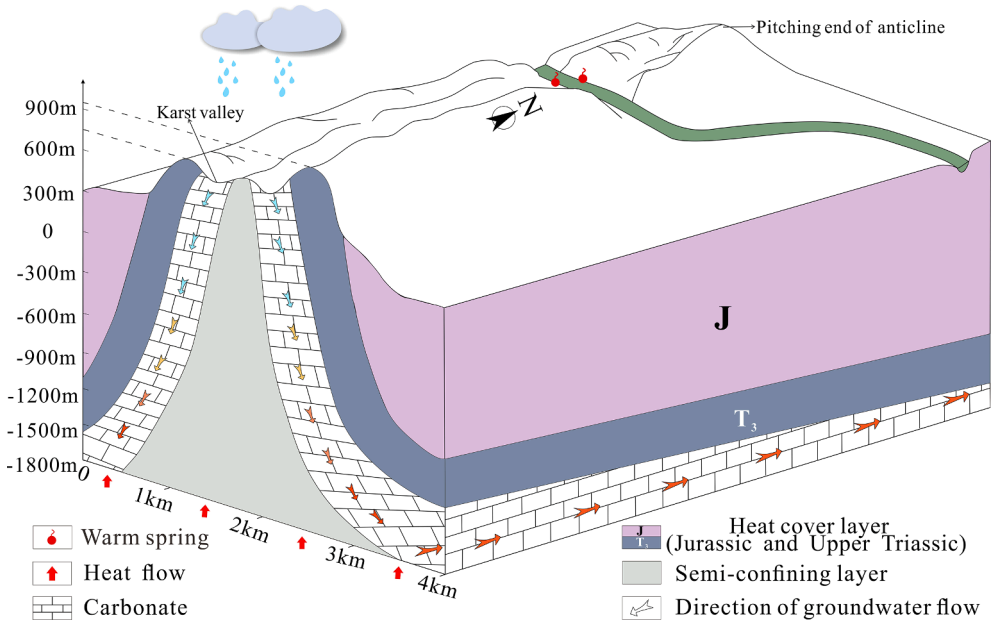

Fig. 9. Conceptual model of the mid-deep groundwater circulation in MWC.

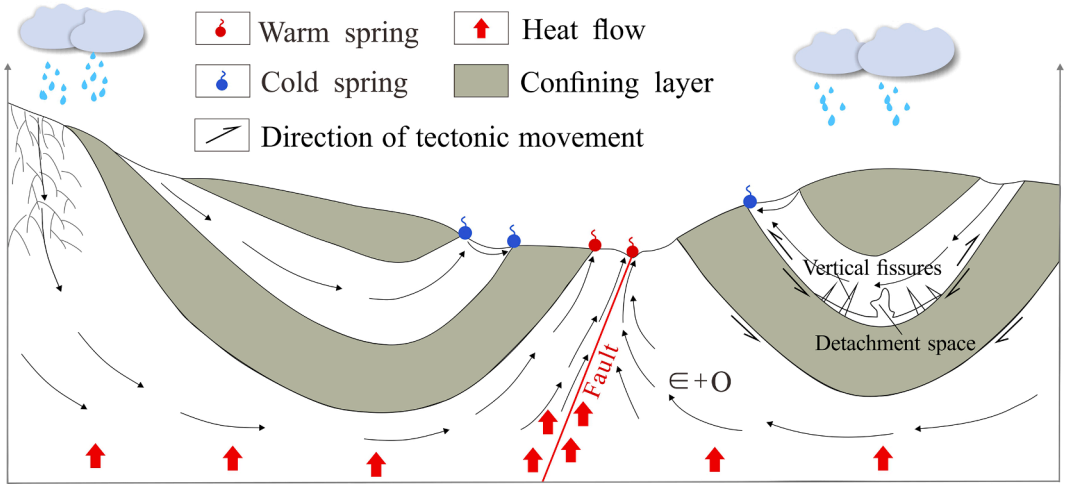

Fig. 10. Conceptual model of the middle-deep groundwater circulation in NEC and SEC.

deposits. The total salt content of the inland fluvial lacustrine Jurassic strata to the west of the Mt. Huaying basement fault is 0.76–20.91%, which has greatly exceeded the salt-bearing formation index (>0.5%) (Li et al., 1980; Xie et al., 1981). However, the strata in the axis of the steeply-dipping anticlines are eroded earlier, and the fissures caused by tensile stress provide ideal channels for fluid flow, resulting in the formation of sulfate-water by leaching and dilution. Salts are precipitated according to their solubility. Sulfate rocks with low solubility are distributed extensively, and it is easy for chlorides to be over-filtrated and diluted, so that sulfate-water is widely distributed.

5.5. Conceptual model of middle-deep groundwater circulation

The deep-seated thermal fluids are principally controlled by stratigraphic structure and topography, while the influence of karst development is significantly weakened (Wang et al., 2018). Boreholes on both sides of the anticlines (e.g., no. 39, 41, 48 and 51) are located at the flexure point of the anticline flank and syncline, and there are still SO_4-Ca type geothermal waters in the reservoirs drilled from the mid-Jurassic to the buried depths of 1718–2974 m (Wang, 2003; Yang et al., 2017; Wang and Zhang, 2004). The Yangtze River, the base level of erosion in study area, is above 150 m.a.s.l. In addition, the drilling profiles in MWC and SEC show that the karst fracture systems of reservoirs are heterogeneous, which are separated into several sections by dense limestone (Liu, 2010). All of these show that the groundwater flows along the deep-seated strata may not be controlled by the minimum erosion base level. Although the shallow aquifer is exposed to the surface at the formation decompression formed by river erosion, groundwater in the deep aquifer continues to flow along the stratum below the river that cuts the core of an anticline and supplies the reservoirs in the flanks of the anticline at the opposite river bank.

The recharge and discharge of groundwater in a basin is generally driven by gravity (Tóth, 1963) and overburden pressure (Lin, 2006). Precipitation in MWC recharges groundwater via tectonically weak zones such as karst valleys in steeply-dipping anticlines and tensile fractures that connect cap rocks and aquifers in anticlines, and the amount of recharge is related to the aquifer's outcrop area. Shallow karst groundwater flows through the aquifer to the depth of the two

flanks of the anticline and along the anticlinal trend towards the plunging end. The Triassic aquifers in the syncline axes are mostly buried at a depth of about 3 km (Han, 2002). Under the action of sedimentary compaction, only solid evaporites and a small amount of stagnant formation water (brine) are retained in deep-seated syncline axes. Most of the brine is compacted and discharged (Ma et al., 1988; Song, 1993; Tang et al., 2018). Compaction also makes the deep-seated carbonates in the syncline axis have low porosity, which impede the fluid movement along the flank of the anticline to the synclinal axis. Groundwater in the two flanks of the same anticline is separated by mudstone and limestone of the Lower Triassic Feixianguan formation in the core, and connects only at the plunging end (Fig. 9).

In the process of deep circulation, chemical heat generated in the process of water–rock interaction and the geothermal gradient make the groundwater temperature increase. Groundwater dissolves surrounding rock minerals and obtains the corresponding chemical components. These waters can be replenished by connate water in the depth of the anticlinal flanks and mixed with shallow groundwater as they discharge at the decompression of rock strata such as anticlines cut by rivers or faults to form a spring (Fig. 9).

The well-developed fractures and decollement spaces formed in the NEC and SEC synclinal cores provide flow paths, and there are parallel axial and vertical axial groundwater flows under the influence of gravity. The depths of carbonate aquifers in synclinal axes are shallower than those in MWC. Driven by gravity associated with the topographic gradients, the meteoric water percolates via karst fissures and faults from higher altitude in the folds. The places with higher altitudes are not limited to anticlines, but may also be the gentle flanks within higher altitudes of synclines. The groundwater flows across the formation and through the synclinal axes to supply the adjacent anticlines, or discharges in areas with topographic head differences and/or fault cutting to form thermal springs. The fluid is heated by geothermal heat, and dissolves evaporites to increase salinity (Figs. 8, 10).

6. Conclusions

The geological structure affects the erosion and weathering of the strata within the geologic structures of Chongqing in southwest China, which makes the evolution and distribution of hydrochemical types and flow paths of groundwater behave according to certain regular patterns. The middle-deep groundwaters in this region mainly dissolve gypsum (and/or anhydrite) or halite to form sulfate-water or chloride-water, respectively. Due to the different degree of structural closure related to topographic relief and the history of geological evolution, these middle-deep groundwaters have undergone all or part of the whole process as marine sedimentary metamorphic brine → flushing out of brines by meteoric water → rainwater mainly dissolving chloride minerals → rainwater mainly dissolving sulfate minerals → rainwater mainly dissolving carbonate minerals.

The tectonic stress transferred from SE to NW in the Jiangnan Orogenic Belt makes the maximum circulation depth of middle-deep groundwater decreasing in the same direction, and the average reservoir temperatures of sulfate-water decrease from SEC (82 ± 15 °C) to MWC (78 ± 9 °C). From the southeast to northwest of SEC, there is a transition from sulfate-water to chloride-water, and its average maximum circulation depths are reduced from 3.2 ± 0.7 to 2.3 ± 0.8 km, and the average estimated reservoir temperatures are reduced from 82 ± 15 to 64 ± 18 °C. The steeply-dipping anticlines in MWC are characterized by the concentration of tectonic stress and the occurrence of sulfate-water due to excessive leaching, while synclines and low anticlines with confined structures or recent weathering and denudation exude chloride-water, and the average maximum circulation depths and temperatures of the former (2.1 ± 0.3 km, 78 ± 9 °C) are higher than those of the latter (1.8 ± 0.3 km, 69 ± 8 °C). The Qinling-Dabie Orogenic Belt in NEC is characterized by tectonic stress transferred from NE to SW. Violent tectonics, thickening of strata, and well-developed fractures result in rapid downward percolation of groundwater and the lowest average estimated reservoir temperature of chloride-water (55 ± 27 °C). Paleozoic strata of the anticlines are exposed by relatively recent denudation hosting chloride-water, and Triassic formations largely outcrop in synclines containing sulfate-water.

Precipitation in MWC recharges groundwater via karst valleys and faults in the axes of steeply-dipping anticlines. Driven by gravity, the total flow direction of middle-deep groundwater is anticlinal plunging end and deep-seated flanks, which cannot cross the deep-seated synclines to discharge or supply another anticline. The structure and geomorphology of NEC and SEC are not consistent, and groundwater replenished by precipitation can discharge or replenish another anticline across the syncline. The folds in the area to the west of the Mt. Huaying basement fault tend to be horizontal, and the groundwater runoff is slow or even stagnant, and there are high salinity brines from leached rock salt or connate deposits. In the process of runoff, the groundwater is heated by geothermal and chemical heat, mixes with different layers while ascending and mostly discharges springs formed in places such as river valleys or faults.

The outflow of eight middle-deep groundwater sampling points in MWC varies slightly with a variation about 9.5% (Luo et al., 2001; Pu et al., 2001; Wang, 2003; Wang and Zhang, 2004; Xiao, 2004; Yang, 2008; Zhang, 2006; Zhang and Pu, 2005). It may be that in groundwater flow systems composed of multiple aquifers and aquitards, well-developed shallow faults lead to the mixing of meteoric water, or that water extraction (groundwater mining) causes the decrease of geothermal reservoir pressure. This may results in cones of depression in some areas that the adjacent aquifers replenish across relatively impermeable layers. This may affect the calculations of reservoir temperature and cycle depth, but establishing that the overall variation trend provides a certain reference value.

CRediT authorship contribution statement

Jieru Zhang: Conceptualization, Methodology, Software, Data curation, Writing – original draft, Writing – review & editing. **Pingheng Yang:** Conceptualization, Methodology, Software, Writing – review & editing, Project administration, Funding acquisition. **Chris Groves:** Writing – review & editing. **Xiaohui Luo:** Investigation, Writing – original draft. **Yuyang Wang:** Data curation, Writing – review & editing.

Declaration of Competing Interest

The authors declare that they have no known competing financial interests or personal relationships that could have appeared to influence the work reported in this paper.

Acknowledgments

The authors thank the three anonymous reviewers for their constructive and valuable comments. This work was supported by the Key Laboratory of Karst Ecosystem and Treatment of Rocky Desertification, Ministry of Natural Resources (Grant no. KDL202102), and the Fundamental Research Funds for the Central Universities (Grant no. XDJK2018AB002).

Appendix

.

Table A1
Major ions and isotopes.

Subregion	Sample no.	Water temperature	pH	K^+	Na^+	Ca^{2+}	Mg^{2+}	HCO_3^-	SO_4^{2-}	Cl^-	Br^-	Sr^{2+}	SiO_2	TDS	δD	$\delta^{18}O$	Hydrochemical faces	T_1	T_2	$T_{K\text{-}Mg}$	$T_{Na\text{-}K\text{-}Ca}$	Z	Well depth(m)	Source
Northeast Chongqing	1	13	8.1	445.0	30100.0	1915.0	484.0	210.0	3135.0	46645.0	0.4	–	5.7	82933	-53.2	-9.9	Na-Cl	22	17	116	136	207	–	Guo, 2019
	2	28	7.7	69.5	10220.6	463.2	52.9	241.1	1206.7	16604.3	7.1	10.8	13.3	28860	-42.9	-9.9	Na	49	48	95	164	1105	–	Zhou et al., 2014
	3	24	7.2	397.1	25066.2	2566.6	586.4	109.4	965.1	44361.4	273.6	–	–	47770	–	–	Na-Cl	–	–	110	108	–	1093	Luo et al., 1981
	4	38	7.0	84.3	3875.1	639.9	133.1	213.5	2173.8	5731.7	–	17.2	31.2	12903	–	–	Na-Cl-SO_4	81	82	88	129	2203	–	Wang et al., 2018
	5	–	7.6	118.0	5650.0	830.0	190.0	208.0	2570.0	8010.0	15.2	–	–	13900	–	–	Na-Cl	–	–	92	127	–	–	Guo, 2019
	6	38	7.2	90.5	3755.0	960.0	177.0	182.0	2060.0	6850.0	0.7	24.0	24.1	14095	–	–	Na-Ca-Cl	71	71	86	104	1854	–	Guo, 2019
	7	19	7.2	1.8	315.2	209.9	45.9	219.3	1009.2	120.1	0.0	–	–	1810	–	–	Na-Ca-SO_4	–	–	19	63	–	–	Luo et al.,
	8	24	7.2	80.4	7157.9	999.8	249.7	223.3	3099.9	11246.5	6.3	–	–	26592	–	–	Na-Cl	–	–	79	104	–	–	1981
	9	24	7.5	2178.3	105866.2	6394.2	1375.5	2994.6	923.8	178230.7	901.7	–	–	300990	–	–	Na-Cl	–	–	150	120	–	941	
	10	20	7.7	222.2	14960.1	1684.8	590.1	301.6	4309.3	24503.4	145.9	–	–	46560	–	–	Na-Cl	–	–	94	111	–	734	
	Min	13	7.0	1.8	315.2	209.9	45.9	109.4	923.8	120.1	0.0	10.8	5.7	1810	–	–		22	17	19	63	207	–	
	Max	38	8.1	2178.3	105866.2	6394.2	1375.5	2994.6	4309.3	178230.7	901.7	24.0	31.2	300990	–	–		81	82	150	164	2203	–	
	Mean	25	7.4	368.7	20696.6	1666.3	388.5	490.3	2145.3	34230.3	150.1	17.3	18.6	57641	–	–		56	55	93	117	1342	–	
	SD	9	0.3	652.4	31445.0	1810.2	403.0	881.2	1146.0	53061.1	297.2	6.6	11.3	88694	–	–		26	29	33	26	885	–	
	11	19	7.1	–	10.8	189.4	47.7	277.6	425.1	14.9	–	–	–	826	–	–	Ca-Mg-SO_4-HCO_3	–	–	–	–	–	–	Luo et al.,
	12	20	7.2	–	6.9	168.3	32.8	253.2	333.8	10.6	–	–	–	679	–	–	Ca-Mg-SO_4-HCO_3	–	–	–	–	–	–	1981
	13	21	7.2	–	9.7	150.9	43.2	237.4	345.8	12.1	–	–	–	688	–	–	Ca-Mg-SO_4-HCO_3	–	–	–	–	–	–	
	Min	19	7.1	–	6.9	150.9	32.8	237.4	333.8	10.6	–	–	–	679	–	–		–	–	–	–	–	–	
	Max	21	7.2	–	10.8	189.4	47.7	277.6	425.1	14.9	–	–	–	826	–	–		–	–	–	–	–	–	
	Mean	20	7.2	–	28633.5	1966.8	41.2	256.1	368.2	12.5	–	–	–	731	–	–		–	–	–	–	–	–	
	SD	1	0.1	–	2.0	19.3	7.6	20.3	49.6	2.2	–	–	–	82	–	–		–	–	–	–	–	–	
Midwest Chongqing	14	38	7.3	178.2	19194.1	1472.8	318.2	196.8	979.4	25963.9	–	–	–	48303	–	–	Na-Cl	–	–	96	116	–	–	
	15	26	8.0	208.6	29334.6	1417.5	431.1	282.1	5499.9	44803.2	–	–	–	81977	–	–	Na-Cl	–	–	96	129	–	–	
	16	37	7.1	187.0	19101.8	1464.0	342.8	188.7	9800.3	25881.8	–	–	–	56966	–	–	Na-Cl-SO_4	–	–	96	118	–	–	
	17	–	7.9	298.0	96000.0	970.0	65.0	247.0	1870.0	199100.0	175.0	–	–	228400	–	–	Na-Cl	–	–	135	208	–	–	Gong, 2016
	18	51	6.8	967.2	38728.0	1759.7	460.1	319.3	5394.6	59272.7	31.0	43.9	26.6	106901	–	–	Na-Cl	74	75	141	187	1984	–	
	19	51	7.3	22.5	999.6	658.4	90.7	214.2	1753.6	1658.6	0.2	13.1	20.2	5397	–	–	Na-Ca-Cl-SO_4	64	64	61	76	1626	–	
	20	–	6.8	794.0	141000.0	1460.0	250.0	117.0	3220.0	225400.0	< 0.05	–	–	323500	–	–	Na-Cl	–	–	145	230	–	–	Gong, 2016
	21	–		632.2	40976.6	4914.8	912.9	40.6	1942.6	73509.4	997.9	–	–	124410	–	–	Na-Cl	–	–	117	89	–	–	Cao, 2019
	22	–	6.7	1430.0	129000.0	1330.0	420.0	117.0	8680.0	296800.0	271.0	–	–	319800	–	–	Na-Cl	–	–	157	304	–	–	Gong,
	23	–	7.7	47.3	812.0	450.0	77.0	221.0	1190.0	2630.0	4.8	–	–	17400	–	–	Na-Ca-Cl-SO_4	–	–	80	115	–	–	2016
	24	–	7.8	920.0	44300.0	5830.0	1150.0	1040.0	2530.0	74400.0	99.9	–	–	126600	–	–	Na-Cl	–	–	125	91	–	–	Guo, 2019
	25	42	7.7	2870.0	126000.0	1170.0	670.0	117.0	9370.0	269400.0	< 0.05	–	–	319300	–	–	Na-Cl	–	–	174	470	–	–	Gong, 2016
	Min	26	6.7	22.5	812.0	450.0	65.0	40.6	979.4	1658.6	< 0.05	13.1	20.2	5397	–	–		64	64	61	76	1626	–	
	Max	51	8.0	2870.0	141000.0	5830.0	1150.0	1040.0	9800.3	296800.0	997.9	43.9	26.6	323500	–	–		74	75	174	470	1984	–	
	Mean	41	7.4	712.9	57120.6	1908.1	432.3	258.4	4352.5	108235.0	225.7	28.5	23.4	146580	–	–		69	70	118	178	1805	–	
	SD	9	0.5	808.8	51520.3	1671.1	335.2	258.4	3312.4	108018.6	354.6	21.8	4.5	120144	–	–		7	8	34	115	253	–	
	26	30	7.5	5.5	2.3	641.5	183.4	132.8	2044.0	62.5	< 0.05	13.8	15.3	3071	–	–	Ca-Mg-SO_4	54	54	26	98	1280	–	Yang et al., 2017
	27	28	7.1	13.5	498.7	522.5	126.1	237.8	1517.1	809.3	0.6	13.2	16.8	3678	–	–	Ca-Na-SO4-Cl	57	57	47	70	1391	–	
	28	42	7.4	13.6	66.3	647.4	150.2	136.5	2129.9	19.1	0.0	17.1	28.0	3381	–	–	Ca-Mg-SO_4	77	77	45	50	2057	–	
	29	–	8.0	2.5	6.5	86.0	19.0	117.0	210.0	93.0	0.2	–	–	360	–	–	Ca-Mg-SO_4-CI-HCO_3	–	–	32	80	–	–	
	30	35	7.7	4.9	11.4	457.9	92.0	213.2	1371.5	11.9	< 0.05	8.3	21.9	2097	–	–	Ca-Mg-SO_4	67	68	30	37	1731	1570	
	31	37	7.5	4.4	6.3	379.3	60.5	223.6	1005.0	2.7	0.1	16.7	22.9	1620	–	–	Ca-Mg-SO_4	69	69	32	38	1786	556	
	32	41	7.0	15.9	3.1	82.5	4.1	150.4	104.1	42.7		4.9	27.5	387	–	–	Ca-HCO_3-SO_4-Cl	76	77	90	131	2029	2053	

(*continued on next page*)

Table A1 (*continued*)

Subregion	Sample no.	Water temperature	pH	K^+	Na^+	Ca^{2+}	Mg^{2+}	HCO_3^-	SO_4^{2-}	Cl^-	Br^-	Sr^{2+}	SiO_2	TDS	δD	$\delta^{18}O$	Hydrochemical faces	T_1	T_2	$T_{K\text{-}Mg}$	$T_{Na\text{-}K\text{-}Ca}$	Z	Well depth(m)	Source
											< 0.12													
	33	44		19.6	96.7	682.1	142.0	215.6	2061.7	188.9	0.2	15.0	23.7	3410	–	–	Ca-Mg-SO_4	70	71	53	57	1833	1853	
	34	51	7.6	22.3	25.2	663.1	115.8	168.3	1910.2	6.8	0.1	17.0	30.8	2904	–	–	Ca-Mg-SO_4	80	81	58	52	2186	1853	
	35	48	7.6	23.4	13.9	641.9	80.4	195.9	1792.6	4.1	0.0	18.1	29.3	2715	–	–	Ca-SO_4	78	79	63	51	2116	1778	
	36	40	7.7	17.5	8.1	651.9	120.0	157.1	1903.2	4.1	0.1	17.6	24.6	2833	-52.1	-7.6	Ca-Mg-SO_4	71	72	53	43	1883	1330	
	37	52	7.5	18.7	13.4	600.5	118.4	166.4	1760.8	2.3	0.1	19.3	32.1	2665	–	–	Ca-Mg-SO_4	82	83	54	49	2246	1910	
	38	33	7.5	9.9	6.3	329.4	145.1	233.3	1219.9	4.1	0.1	13.0	20.6	1895	–	–	Ca-Mg-SO_4	65	65	39	54	1651	700	
	39	57	7.3	17.7	20.5	614.8	109.7	183.5	1843.5	11.2	0.1	18.2	31.8	2775	–	–	Ca-Mg-SO_4	82	83	54	50	2230	1718	
	40	50	7.7	22.3	46.6	604.7	109.4	160.2	1945.2	9.6	0.0	17.6	26.1	2875	–	–	Ca-Mg-SO_4	74	75	59	59	1962	1866	
	41	55	7.4	23.2	36.8	549.0	85.2	174.2	1652.8	8.2	0.0	18.4	32.6	2508	–	–	Ca-SO_4	83	84	62	62	2264	2336	
	42	48	7.7	21.9	52.9	535.8	90.1	186.6	1576.5	24.0	0.1	15.7	34.4	2458	–	–	Ca-Mg-SO_4	85	86	60	64	2343	349	
	43	53	8.2	23.2	47.6	547.6	81.4	169.1	1634.4	26.0	0.1	16.8	36.2	2530	–	–	Ca-SO_4	87	88	63	64	2414	118	
	44	52	7.6	8.8	27.8	358.3	71.6	219.5	1042.9	19.6	0.1	12.7	27.9	1710	–	–	Ca-Mg-SO_4	76	77	44	58	2051	2178	
	45	41	7.3	11.7	44.9	585.6	122.9	195.9	1711.2	43.7	0.2	16.3	26.2	2686	-60.1	-9.1	Ca-Mg-SO_4	74	75	44	49	1968	227	
	46	41	7.4	12.5	55.4	623.8	166.6	171.1	1982.0	45.1	0.2	16.2	34.4	3035	–	–	Ca-Mg-SO_4	85	86	42	49	2343	518	
	47	38	8.4	12.9	52.3	641.9	128.6	162.7	1983.3	46.4	0.3	16.5	35.2	3030	–	–	Ca-Mg-SO_4	86	87	46	49	2376	701	
	48	53	7.0	10.9	56.4	606.5	142.2	179.6	1956.1	32.1	< 0.05	9.8	32.0	2974	-63.8	-9.3	Ca-Mg-SO_4	82	83	41	48	2238	2062	
	49	52	7.7	12.9	39.3	575.6	131.5	170.4	1731.0	26.6	0.2	16.6	26.2	2660	–	–	Ca-Mg-SO_4	74	75	45	51	1968	1981	
	50	57	7.6	16.1	44.7	594.1	90.1	194.4	1716.3	24.6	0.2	16.6	34.0	2650	–	–	Ca-SO_4	85	85	54	54	2324	1918	
	51	50	7.7	23.1	170.1	509.2	114.5	159.2	1676.3	109.2	0.3	17.0	40.7	2758	–	–	Ca-Mg-SO_4	92	93	59	75	2586	2156	
	52	45	7.7	10.4	17.4	541.1	108.1	212.7	1514.2	10.9	0.1	15.6	26.2	2362	–	–	Ca-Mg-SO_4	74	75	43	45	1968	418	
	53	42	7.6	10.4	34.6	599.4	119.0	188.2	1840.3	24.6	0.3	16.5	31.1	2780	–	–	Ca-Mg-SO_4	81	82	42	45	2199	188	
	54	40	7.7	9.7	35.1	697.6	59.5	186.6	1840.3	21.9	0.2	16.4	31.0	2816	–	–	Ca-SO_4	81	82	48	40	2196	71	
	55	55	7.7	15.9	22.5	625.9	130.6	168.0	2048.2	10.4	0.1	15.8	40.7	3008	-57.4	-8.4	Ca-Mg-SO_4	92	93	50	48	2586	173	
	56	52	7.9	15.2	22.7	668.4	86.8	171.1	1977.0	9.6	0.2	15.7	39.8	2936	-57.6	-8.1	Ca-SO_4	91	92	53	46	2552	126	
	57	48	7.5	3.7	7.6	243.5	47.6	160.1	659.3	7.5	–	6.1	36.3	1193	–	–	Ca-Mg-SO_4	87	88	31	49	2417	–	Yang et al.,
	58	39	7.2	7.7	12.5	250.2	57.6	183.8	717.3	14.4	–	8.0	28.4	1212	–	–	Ca-Mg-SO_4	77	78	43	64	2073	–	2019
	Min	28	7.0	2.5	2.3	82.5	4.1	117.0	104.1	2.3	< 0.05	4.9	15.3	360	-63.8	-9.3		54	54	26	37	1280	–	
	Max	57	8.4	23.4	498.7	697.6	183.4	237.8	2129.9	809.3	0.6	19.3	40.7	3678	-52.1	-7.6		92	93	90	131	2586	–	
	Mean	45	7.6	14.0	48.7	526.0	103.3	180.1	1578.1	53.8	0.1	14.9	29.5	2484	-58.2	-8.5		78	79	49	56	2102	–	
	SD	8	0.3	6.3	87.1	164.5	39.8	28.4	522.8	140.7	0.1	3.7	6.3	787	4.3	0.7		9	9	12	18	313	–	
Southeast Chongqing	59	43	7.0	68.5	3373.9	617.3	127.3	128.9	1668.7	5626.0	0.4	16.1	26.0	11620	-62.1	-9.2	Na-Cl	74	74	83	123	2828	40	Yang et al.,
	60	43	7.1	68.8	3406.5	624.9	134.4	119.7	1627.1	5589.6	< 0.05	16.2	26.4	11611	–	–	Na-Cl	74	75	82	122	2859	1866	2019
	61	–		298.5	14067.2	883.7	240.3	225.2	2789.9	21894.9	–	15.2	–	40410	–	–	Na-Cl	–	–	114	179	–	–	Zhou et al., 1980
	62	23	7.2	171.9	8159.7	680.0	128.0	178.8	1953.3	12616.0	0.9	19.9	21.7	23867	–	–	Na-Cl	67	67	107	167	2487	–	Yang et al., 2019
	63	–		176.0	2767.3	256.1	65.1	195.8	681.2	4140.7	–	–	–	8170	–	–	Na-Cl	–	–	118	295	–	–	Zhou et al., 1980
	64	–		290.6	10006.2	707.2	184.3	210.9	2206.3	15726.8	–	–	–	29330	–	–	Na-Cl	–	–	117	198	–	–	Zhou et al., 1980
	65	18	7.8	35.2	1398.9	178.5	30.3	203.4	348.8	2183.9	0.4	3.5	10.1	4305	-41.8	-7.0	Na-Cl	39	38	84	197	1144	–	Yang et al.,
	66	19	7.4	104.9	5194.4	457.6	20.2	210.3	936.4	8017.7	0.6	13.0	15.4	14883	–	–	Na-Cl	54	54	120	175	1865	–	2019
	67	22	7.2	74.4	2825.6	70.8	201.0	219.6	646.1	4610.4	–	9.3	13.1	8691	–	–	Na-Cl	48	48	79	719	1588	–	
	68	53	7.1	66.5	2250.0	466.4	3.0	172.9	1129.7	3477.3	2.5	20.3	38.2	7590	–	–	Na-Cl	90	90	136	138	3590	–	
	Min	18	7.0	35.2	1398.9	70.8	3.0	119.7	348.8	2183.9	0.4	3.5	10.1	4305	-62.1	-9.2		39	38	79	122	1144	–	
	Max	53	7.8	298.5	14067.2	883.7	240.3	225.2	2789.9	21894.9	2.5	20.3	38.2	40410	-41.8	-7.0		90	90	136	719	3590	–	
	Mean	32	7.3	135.5	5345.0	494.2	113.4	186.6	1398.7	8388.3	1.0	14.2	21.5	16048	-52.0	-8.1		64	64	104	231	2337	–	
	SD	14	0.3	95.5	4103.3	258.6	81.5	36.8	781.0	6365.6	0.9	5.6	9.7	11534	14.4	1.5		17	18	20	179	848	–	
	69	42	8.0	6.4	6.6	123.7	48.0	198.0	328.2	5.5	< 0.05	6.7	27.8	668	-62.0	-9.1	Ca-Mg-SO_4-HCO_3	76	77	41	86	2953	–	Yang et al., 2019

(*continued on next page*)

Table A1 (*continued*)

Subregion	Sample no.	Water temperature	pH	K^+	Na^+	Ca^{2+}	Mg^{2+}	HCO_3^-	SO_4^{2-}	Cl^-	Br^-	Sr^{2+}	SiO_2	TDS	δD	$\delta^{18}O$	Hydrochemical faces	T_1	T_2	T_{K-Mg}	$T_{Na-K-Ca}$	Z	Well depth(m)	Source
	70	35	7.3	7.0	8.9	186.0	36.1	113.1	533.2	2.8	< 0.05	12.0	30.8	848	-61.0	-9.2	Ca-Mg-SO_4	80	81	46	71	3155	–	
	71	47	7.6	18.8	191.7	224.7	29.1	170.9	539.0	282.5	< 0.05	6.3	66.2	1472	-61.7	-9.2	Ca-Na-SO_4-Cl	115	116	70	115	4806	–	
	72	54	7.6	3.6	3.7	62.4	16.8	165.5	93.7	4.3	–	0.9	29.8	396	–	–	Ca-Mg-SO_4-HCO_3	79	80	40	102	3092	1645	
	73	43	8.0	0.7	0.1	57.8	21.8	151.8	87.6	4.4	0.3	0.7	16.8	276	-65.0	-9.7	Ca-Mg-SO_4-HCO_3	57	57	9	47	2023	1456	
	74	35	7.4	8.6	5.0	497.8	98.9	125.5	1511.2	3.4	–	12.6	33.4	2268	-64.3	-9.5	Ca-Mg-SO_4	84	85	40	39	3316	–	
	75	37	7.1	8.1	2.1	500.2	114.4	130.5	1519.8	1.8	< 0.05	13.9	31.7	2305	-63.3	-9.7	Ca-Mg-SO_4	82	83	38	34	3214	–	
	76	39	7.3	2.1	4.7	99.9	2.5	226.4	83.2	3.0	0.1	11.2	30.7	366	-52.7	-8.3	Ca-HCO_3-SO_4	80	81	49	68	3149	–	
	77	48	7.1	9.6	2.7	277.4	43.4	169.7	698.4	4.5	0.1	11.5	42.6	1196	-56.0	-8.5	Ca-Mg-SO_4	95	95	51	55	3822	–	
	78	35	7.6	0.9	0.6	59.2	24.3	247.1	56.1	0.4	0.1	7.8	23.9	408	-50.0	-7.9	Ca-Mg-SO_4-HCO_3	70	71	13	60	2664	–	
	Min	35	7.1	0.7	0.1	57.8	2.5	113.1	56.1	0.4	0.1	0.7	16.8	276	-65.0	-9.7		57	57	9	34	2023	–	
	Max	54	8.0	18.8	191.7	500.2	114.4	247.1	1519.8	282.5	0.3	13.9	66.2	2305	-50.0	-7.9		115	116	70	115	4806	–	
	Mean	42	7.5	6.6	22.6	208.9	43.5	169.9	545.0	31.3	0.2	8.4	33.4	1020	-59.6	-9.0		82	83	40	68	3219	–	
	SD	7	0.3	5.4	59.5	169.8	35.9	43.5	559.7	88.3	0.1	4.7	13.3	770	5.4	0.6		15	15	18	26	725	–	

The water temperature and reservoir temperature (T) are in °C; the concentrations of major ions and TDS are in mg/L; δ18O, δD values are in ‰; The circulation depth (Z) is in m; The reservoir temperature (T) is in °C; – denotes no datum.

References

Arnorsson, S., 1985. The use of mixing models and chemical geothermometers for estimating underground temperatures in geothermal systems. J. Volcanol. Geoth. Res. 23, 299–335. https://doi.org/10.1016/0377-0273(85)90039-3.

Chadha, D.K., 1999. A proposed new diagram for geochemical classification of natural waters and interpretation of chemical data. Hydrogeol. J. 7 (5), 431–439. https://doi.org/10.1007/s100400050216.

Choi, B.Y., Yun, S.T., Mayer, B., Hong, S.Y., Kim, K.H., Jo, H.Y., 2012. Hydrogeochemical processes in clastic sedimentary rocks, South Korea: A natural analogue study of the role of dedolomitization in geologic carbon storage. Chemical Geol. 306, 103–113. https://doi.org/10.1016/j.chemgeo.2012.03.002.

Coomar, P., Mukherjee, A., Bhattacharya, P., Bundschuh, J., Verma, S., Fryar, A.E., Ramos, O.E.R., Munoz, M.O., Gupta, S., Mahanta, C., Quino, I., Thunvik, R., 2019. Contrasting controls on hydrogeochemistry of arsenic-enriched groundwater in the homologous tectonic settings of Andean and Himalayan basin aquifers, Latin America and South Asia. Sci. Total. Environ. 689, 1370–1387. https://doi.org/10.1016/j.scitotenv.2019.05.444.

Chen, X.C., 1977. Regional hydrogeological survey report in Chengkou (plotting scale 1: 200,000) (in Chinese).

Chen, K.G., Li, L., Li, C.M., et al., 2014. Evolution of the potash–rich areas in evaporation basin during the epigenetic stage with continental block being active. Prog. Earth Sci. 29 (4), 515–522. https://doi.org/10.11867/j.issn.1001-8166.2014.04.0515 (in Chinese with English abstract).

Chen, Z.Y., Li, Q.M., Xia, B., 2007. Mechanism and accumulation effect of thermochemical sulfate reduction in northeast area of Sichuan basin. Nat. Gas Geosci. 5, 743–749. https://doi.org/10.3969/j.issn.1672-1926.2007.05.022 (in Chinese with English abstract).

Cheng, Q., Yang, H.L., Zeng, M., 2015. Formation and Protection of karst geothermal water resources in Chongqing. Carsologica Sinca 34 (03), 217–227. https://doi.org/10.11932/karst20150303 (in Chinese with English abstract).

Cao, Q., 2014. Hydrochemical characteristics and origins of the deep–formation brines and hot springs occurring in the Triassic strata in high–fold belts of the eastern Sichuan basin. China Univ. of Geosci, Beijing (in Chinese with English abstract).

Chongqing Municipal People's Government, 2010. Geological survey report of Chongqing, the capital of Warm Spring in China. Chongqing Municipal People's Government, Chongqing (in Chinese).

Christina, M., Reinhard, N., Baumann, T., 2014. Hydrochemistry and hydrogen sulfide generating processes in the Malm aquifer, Bavarian Molasse Basin. Germany. Hydrogeol. J. 22, 151–162. https://doi.org/10.1007/s10040-013-1064-2.

Craig, H., 1961. Isotopic variations in meteoric waters. Science 133, 1833–1834. https://doi.org/10.1126/science.133.3465.1702.

Craig, H., 1969. Source fluids for the Salton Sea geothermal system. Am. J. Sci. 267, 249–255. https://doi.org/10.2475/ajs.267.2.249.

Drogue, C., Cat, N.N., Dazy, J., 2000. Geological Factors affecting the chemical characteristics of the thermal waters of the carbonate karstified aquifers of Northern Vietnam. Hydrol. Earth Syst. Sci. 4 (2), 322–340. https://doi.org/10.5194/hess-4-332-2000.

Dafny, E., Burg, A., Gvirtzman, H., 2010. Effects of Karst and geological structure on groundwater flow: The case of Yarqon-Taninim Aquifer. Israel. J. Hydrol. 28 (5), 453–472. https://doi.org/10.1016/j.jhydrol.2010.05.038.

Feng, M., An, M.J., Wu, Z.H., et al., 2019. Focal mechanisms of earthquakes in Chongqing and geodynamical implications. Acta Geoscientica Sinica 40 (2), 319–328. https://doi.org/10.3975/cagsb.2018.070201 (in Chinese with English abstract).

Fontes, J.C., Matray, J.M., 1993. Geochemistry and origin of formation brines from the Paris Basin, France: brines associated with Triassic salts. Chemical Geol. 109, 149–175. https://doi.org/10.1016/0009-2541(93)90068-T.

Fournier, R.O., Potter, R.W., 1995. Magnesium Correction to the Na-K-Ca Chemical Geothermometer. J. Hydrol. 172, 31–59. https://doi.org/10.1016/0022-1694(95)02748-E.

Fournier, R.O., 1977. Chemical geothermometers and mixing models for geothermal systems. Geothermics 5 (1–4), 41–50. https://doi.org/10.1016/0375-6505(77)90007-4.

Fournier, R.O., Truesdell, A.H., 1973. An empirical Na-K-Ca geothermometer for natural waters. Geochim. Cosmochim. Acta 37, 1255–1275. https://doi.org/10.1016/0016-7037(73)90060-4.

Fan, J.J., Jia, X.F., Hu, Q.Y., et al., 2014. Potential and suitable conditions evaluation of CO_2 storage in the salt water aquifer in the depth of Sichuan Basin. Groundwater 36 (6), 59–63. https://doi.org/10.3969/j.issn.1004-1184.2014.06.021 (in Chinese with English abstract).

Górecki, W., Sowiżdżał, A., Hajto, M., et al., 2015. Atlases of geothermal waters and energy resources in Poland. Environ Earth Sci 74, 7487–7495. https://doi.org/10.1007/s12665-014-3832-2.

Gao, B.Y., Liang, Y.P., Wang, W.T., 2008. Features of karst water and geologic background in Liulin spring basin. Carsologica Sinca 27 (3), 219–225. https://doi.org/10.3969/j.issn.1001-4810.2008.03.003 (in Chinese with English abstract).

Giggenbach, W.F., 1988. Geothermal solute equilibria. Derivation of Na-K-Mg-Ca geoindicators. Geochim. Cosmochim. Acta 52, 2749–2765. https://doi.org/10.1016/0016-7037(88)90143-3.

Gong, D.X., 2016. Triassic salt–forming environment, Potassium forming conditions and genetic mechanism in Sichuan Basin. Chengdu Univ. of Technology (in Chinese with English abstract).

Guo, J., Zhou, X., Wang, L.D., et al., 2018. Hydrogeochemical characteristics and sources of salinity of the springs near Wenquanzhen in the eastern Sichuan Basin. China. Hydrogeol. J. 26, 1137–1151. https://doi.org/10.1007/s10040-017-1692-z.

Guo, J., 2019. Hydrogeochemical characteristics and evolution of saline/salty springs and subsurface brines in the northeastern Sichuan Basin. China Univ. of Geosciences, Beijing (in Chinese with English abstract).
Guo, X.M., 2015. Accumulation conditions and favorable exploration zones of shale gas in Wufeng-Longmaxi Formation. Chengdu Univ. of Technology, Northeast of Chongqing (in Chinese with English abstract).
Huang, F., Ljiljana, V., Wu, X., et al., 2019. Hydrochemical features and their controlling factors in the Kucaj-Beljanica Massif, Serbia. Environ. Earth Sci. 78, 498. https://doi.org/10.1007/s12665-019-8452-4.
Hu, L.Y., 2017. Tectonics characteristics and its effect on shale gas enrichment in the regional of southeastern Chongqing. China Univ. of Mining and Technology (in Chinese with English abstract).
Hem, J.D., 1970. Study and interpretation of chemical characteristics of natural water. U. S. Survey, Water Supply Paper 1473, 363. https://doi.org/10.3133/wsp1473.
Hao, Y.L., Pang, Z.H., Kong, Y.L., et al., 2020. Chemical and isotopic constraints on the origin of saline waters from a hot spring in the eastern coastal area of China. Hydrol. J. https://doi.org/10.1007/s10040-020-02199-7.
John, W.L., Tonya, L.B., 2016. Direct utilization of geothermal energy 2015 worldwide review. Geothermics. 60, 66–93. https://doi.org/10.1016/j.geothermics.2015.11.004.
Han, H., 2002. Feasibility study report of geothermal resource development in Taojia Town. Jiulongpo District, Chongqing (in Chinese).
Kong, Y.L., Pang, Z.H., Pang, J.M., Lyu, M., Pan, S., 2020. Fault-affected fluid circulation revealed by hydrochemistry and isotopes in a large-scale utilized geothermal reservoir. Geofluids 2020, 2604025. https://doi.org/10.1155/2020/2604025.
Krouse, H.R., Viau, C.A., 1988. Chemical and isotopic evidence of thermochemical sulfate reduction by light hydrocarbon gases in deep carbonate reservoirs. Nature 333, 415–419. https://doi.org/10.1038/333415a0.
Labat, C., Larroque, F., de Grissac, B., Dupuy, A., Saltel, M., Bourbon, P., 2021. Influence of an anticline structure on hydrogeological functioning and aquifer interactions in a multilayered aquifer system: the case of Villagrains-Landiras anticline (Gironde, France). Hydrogeol J 29 (5), 1711–1732. https://doi.org/10.1007/s10040-021-02333-z.
Li, J.K., He, Y.C., Ma, W.D., 1980. Regional hydrogeological survey report of Suining (scale 1:200,000) (in Chinese).
Li, Y.C., Ma, W.D., Wu, M.S., 1977. Regional hydrogeological survey report of Neijiang (scale 1:200,000) (in Chinese).
Li, T.Y., Li, H.C., Shen, C.Z., et al., 2010. Study on the δD and $\delta^{18}O$ characteristics of meteoric precipitation during 2006–2008 in Chongqing, China. Adv. Water Sci. 21 (6), 757–764. https://doi.org/10.14042/j.cnki.32.1309.2010.06.001 (in Chinese with English abstract).
Lin, Y.W., 1993. A discussion of the relation of circulation depth of hot spring water to seismic activity on the northern segment of the Honghe fault zone. Seismology and Geology 15 (3), 193–206 (in Chinese).
Lin, Y.T., 1999. Storage characteristics of the ground brine of Trais is Sichuan basin and the determination factors of its enrichment. J. Salt Lake Res. 3, 1–7. https://doi.org/10.3969/j.issn.1008-858X.1999.03.001 (in Chinese).
Lin, Y.T., Pan, Z.R., 2001. Study on density and torming dassification of gas field brine. J. Salt Lake Res. 9 (3), 1–7. https://doi.org/10.3969/j.issn.1008-858X.2001.03.001 (in Chinese with English abstract).
Lin, Y.T., 2006. On the hydrogeological conditions of groundwater in the Triassic system of Sichuan Basin. J. Salt Lake Res. 1, 1–8. https://doi.org/10.3969/j.issn.1008-858X.2006.01.001 (in Chinese with English abstract).
Lin, J.F., 2016. Early Triassic sedimentary and tectonic setting in Chengkou-Wuxi Areas. South Daba Mountain. China University of Geosciences, Beijing (in Chinese with English abstract).
Liu, B.X., 2010. Summary report on the investigation of geothermal resources in Heishan Valley. Wansheng District, Chongqing (in Chinese).
Lowenstein, T.K., Hardie, L.A., Timofeeff, M.N., et al., 2003. Secular variation in seawater chemistry and the origin of calcium chloride basin brine. Geology 31, 857–860. https://doi.org/10.1130/G19728R.1.
Luo, X.K., Ma, Y.Q., Guan, Z.H., Xiao, M.Z, Yang, Y.H., 1981. Regional hydrogeological survey report of Fengjie (scale1:200,000) (in Chinese).
Luo, X.K., Wang, J.P, Xiao, Z.L., Zhang, Y.L., 2001. Investigation and evaluation report of Chongqing Haitangxiaoyue Heat mine (in Chinese).
Luo, J.X., He, Y.B., 2014. Characteristics of Permian source rocks in the Middle and upper Yangtze region. Nat. Gas Geosci. 25 (9), 1416–1425. https://doi.org/10.11764/j.issn.1672-1926.2014.09.1416 (in Chinese with English abstract).
Luo, X.K., 1987. A preliminary study on the development and utilization of underground hot water in Chongqing. Acta Geologica Sichuan 1, 58–65 (in Chinese).
Luo, Y.J., Liu, D.Y., Xu, M., 2006. Study on the geothermal water runoff in Chongqing. Earth and Environ. 34 (1), 49–54. https://doi.org/10.14050/j.cnki.1672-9250.2006.01.009 (in Chinese with English abstract).
Luo, D., Yang, P.H., Wang, Z.X., et al., 2019. Formation characteristics of carbonate thermal water controlled by fault in southeastern Chongqing. Carsologica Sinca 38 (5), 670–681. https://doi.org/10.11932/karst20190503 (in Chinese with English abstract).
Mou, C.L., Ge, X.Y., Xu, X.S., et al., 2014. Lithofacies palaeogeography of the Late Ordovician and its petroleum geological significance in Middle-Upper Yangtze region. J. Palaeogeog. 16 (4), 427–440. https://doi.org/10.7605/gdlxb.2014.04.036 (in Chinese with English abstract).
Machel, H.G., Krouse, H.R., Riciputi, L.R., et al., 1995. Devonian Nisku sour gas play, Canada: A unique natural laboratory for study of thermochemical sulfate reduction. Am. Chem. Soc. 612, 439–454. https://doi.org/10.1021/bk-1995-0612.ch025.
Ma, K.Y., Jiang, M., Lin, C.L., 1988. Study on the relationship between the depth and shallow strata geological structure and salt basin distribution in Northeast Sichuan. Collection of Institute of Mineral Deposit Geology, Chinese Academy of Geological Sciences (21). Geological Society of China 12 (in Chinese).
Mayo, A.L., Loucks, M.D., 1995. Solute and Isotopic Geochem. and Groundwater flow in the central wasatch range, UTAH. J. Hydrol. 172 (1–4), 31–59. https://doi.org/10.1016/0022-1694(95)02748-E.
Marghade, D., Malpe, D.B., Duraisamy, K., Patil, P.D., Li, P.Y., 2020. Hydrogeochemical evaluation, suitability, and health risk assessment of groundwater in the watershed of Godavari basin, Maharashtra. Central India. Environ. Sci. Pollut. Res. 28 (15), 18471–18494. https://doi.org/10.1007/s11356-020-10032-7.
McIntosh, J.C., Ferguson, G., 2021. Deep meteoric water circulation in Earth's crust. Geophys. Res. Letters 48, 1–10. https://doi.org/10.1029/2020GL090461.
Pang, Z.H., Kong, Y.L., Shao, H.B., Kolditz, O., 2018. Progress and perspectives of geothermal energy studies in China: from shallow to deep systems. Environmental Earth Sciences 77, 580. https://doi.org/10.1007/s12665-018-7757-z.
Parkhurst, D.L., Appelo, C., 2013. Description of Input and Examples for PHREEQC Version 3: A Computer Program for Speciation, Batch-Reaction, One-Dimensional Transport, and Inverse Geochemical Calculations. US Geological Surv, Reston, VA, USA.
Pu, D.L., Wang, J.P., Han, H., 2001. Investigation and evaluation report of Bayeshan Hot ore water source area in Tongliang County, Chongqing (in Chinese).
Pu, J.B., Yuan, D.X., Jiang, Y.J., et al., 2010. Hydrogeochemistry and environmental meaning of Chongqing subterranean karst streams in China. Adv. Water Sci. 21 (5), 628–636. https://doi.org/10.14042/j.cnki.32.1309.2010.05.008 (in Chinese).
Ryabtsev, A.D., Kotsupalo, N.P., Kurakov, A.A., Nemkov, N.M., Vakhromeev, A.G., 2020. Rational use of multicomponent brines extracted together with oil. Theoretical Found. Chemical Eng. 54 (4), 756–761. https://doi.org/10.1134/S0040579520040119.
Richard, A., Banks, D.A., Mercadier, J., Boiron, M.C., Cuney, M., Cathelineau, M., 2011. An evaporated seawater origin for the ore-forming brines in unconformity-related uranium deposits (Athabasca Basin, Canada): Cl/Br and delta Cl-37 analysis of fluid inclusions. Geochim. Cosmochim. Acta 75 (10), 2792–2810. https://doi.org/10.1016/j.gca.2011.02.026.
Schmoker, J.W., Halley, R.B., 1982. Carbonate porosity versus depth: A predictable relation for south Florida. AAPG Bull. 66 (12), 2561–2570. https://doi.org/10.1306/03b5ac73-16d1-11d7-8645000102c1865d.
Shen, J. et al., 2010. Lacustrine deposition and environmental evolution. Science press (in Chineses).
Song, G.F., 1993. Development and utilization of salt resources in Wan County area of Sichuan. China Well and Rock Salt 4, 21–23 (in Chinese).
Soraya, K., Nozar, S., Zargham, M., 2019. Characterization of Semnan thermal springs using principal component analysis and geochemical inverse modeling. Arabian J. Geosciences 12, 777. https://doi.org/10.1007/s12517-019-4957-0.
Sowiżdżał, A., Chmielowska1, A., Tomaszewska1, B., Operacz, A., Chowaniec, J., 2019. Could geothermal water and energy use improve living conditions? Environmental effects from Poland. Arch. Environ. Prot. 45 (3), 109–118. https://doi.org/10.24425/aep.2019.127985.
Stiller, M., Rosenbaum, J.M., Nishri, A., 2009. The origin of brines underlying Lake Kinneret. Chemical Geol. 262 (3–4), 293–309. https://doi.org/10.1016/j.chemgeo.2009.01.030.
Tan, K.O., 1990. Earthquake and geothermal activity in Jiangbei area of Chongqing. J. Geol. Hazards and Environ. Preservation 2, 54–60 (in Chinese).
Ta, M.M., Zhou, X., Guo, J., et al., 2018. Distribution and cause of Chongqing hot spring and underground hot water. Hydrogeol. Eng. Geol. 45 (01), 165–172. https://doi.org/10.16030/j.cnki.issn.1000-3665.2018.01.24 (in Chinese with English abstract).
Ta, M.M., Zhou, X., Guo, J., et al., 2019. Hydrogeochemical Science characteristics and formation of the hot springs occurring in the plunging ends of an anticline in Chongqing, Eastern Sichuan Basin. China. Environ. Earth Sci. 78 (15), 468. https://doi.org/10.1007/s12665-019-8486-7.
Tang, Q.M., Zhang, X., Zhu, Z.J., et al., 2018. Chlorine isotopic composition and potash–forming indicator of halites of the Triassic Jialingjiang Formation in the Dianjiang depression, eastern Sichuan basin. Acta Geol. Sin. 92 (8), 1671–1679. https://doi.org/10.3969/j.issn.0001-5717.2018.08.009 (in Chinese with English abstract).
Tóth, J., 1963. A theoretical analysis of groundwater flow in small drainage basins. J. Geophys. Res. 68 (16), 4795–4812. https://doi.org/10.1029/Jz068i008p02354.
Vengosh, A., Helvaci, C., Karamanderesi, I.H., 2002. Geochemical constraints for the origin of thermal waters from western Turkey. Appl. Geochem. 17 (3), 163–183. https://doi.org/10.1016/S0883-2927(01)00062-2.
Verma, S.P., Santoyo, E., 1997. New improved equations for Na/K, Na/Li and SiO_2 geothermometers by outlier detection and rejection. J. Volcanol. Geoth. Res. 79, 9–23. https://doi.org/10.1016/S0377-0273(97)00024-3.
Wang, D.S., 1989. Stable isotope study on the origin of yellow and black halides in Sichuan Basin. Hydrogeol. Eng. Geol. 2, 21–24. https://doi.org/10.13745/j.esf.yx.2017-5-16 (in Chinese).
Wang, J.P., 2003. Development and Utilization scheme of Lujiao Hot Spring Geothermal Water resources in Banan District, Chongqing (in Chinese).
Wang, Z.X., Zhang, Y.L., 2004. Investigation and Evaluation report of Lishuwan Geothermal Water resources in Shapingba District, Chongqing (in Chinese).
Wang, X.L., Zhou, J.C., Chen, X. et al., 2017. Formation and Evolution of Jiangnan orogenic belt. Bull. Mineralogy, Petrology Geochem. 36 (05), 714–735+696. (in Chinese with English abstract) doi:10.3969/j.Issn.1007-2802.2017.05.003.
Wang, G.L., et al., 2018. Geothermal records of China (Volume 1, Southwest), first ed. Science Press, Beijing (in Chinese).
Warren, J.K., 2010. Evaporites through time, Tectonic, climatic and eustatic controls in marine and nonmarine deposits. Earth Sci. Rev. 98, 217–268. https://doi.org/10.1016/j.earscirev.2009.11.004.

Xia, P.C., Chen, H.L., Chen, J.Q., 1979. Regional Hydrogeological Survey Report of Youyang (scale 1:200,000) (in Chinese).
Xiao, Z.S., 2004. Development and utilization plan of Wangjiang Geothermal water resources in Guojiatuo. Jiangbei District, Chongqing (in Chinese).
Xiao, Q., 2012. Study on the genesis of Triassic carbonate rocks and the process of water–rock interaction in Chongqing. Southwest university (in Chinese).
Xie, Y.X., Tan, K.O., Zuo, Z.H., 1981. Regional Hydrogeological Survey Report of Guangan (scale 1:200,000) (in Chinese).
Xu, M., Zhu, C.Q., Tian, Y.T., Rao, S., Hu, S.B., 2011. Borehole temperature measurement and current geothermal characteristics in Sichuan Basin. Chin. J. Geophysics 54 (4), 1052–1060. https://doi.org/10.3969/j.issn.0001-5733.2011.04.020 (in Chinese).
Yan, D.P., Qiu, L., Chen, F., et al., 2018. Structural style and kinematics of the Mesozoic Xuefengshan intraplate orogenic belt. Earth Sci. Frontiers 25 (01), 1–13. https://doi.org/10.13745/j.esf.yx.2017-5-16 (in Chinese with English abstract).
Yang, P.H., Luo, D., Hong, A.H., et al., 2019b. Hydrogeochemistry and geothermometry of the carbonate-evaporite aquifers controlled by deep-seated faults using major ions and environmental isotopes. J. Hydrol. 579, 124116 https://doi.org/10.1016/j.jhydrol.2019.124116.
Yang, H.L., Zhang, Y.L., Wang, J.P., Chen, S.Y., 2007. An Evaluation report of geothermal resources in Banan District, Chongqing—the hometown of hot springs in China (in Chinese).
Yang, H.Y., 2008. Geothermal water resources evaluation report of Tongjing Town. Yubei District, Chongqing (in Chinese).
Yang, P.H., Cheng, Q., Xie, S.Y., et al., 2017. Hydrogeochemistry and geothermometry of deep thermal water in the carbonate formation in the main urban area of Chongqing, China. J. Hydrol. 549, 50–61. https://doi.org/10.1016/j.jhydrol.03.054.
Yang, P.H., Luo, D., Groves, C., Xie, S.Y., 2019. Geochem. and genesis of geothermal well water from a carbonate-evaporite aquifer in Chongqing, SW China. Environ. Earth Sci. 78, 33. https://doi.org/10.1007/s12665-018-8004-3.
Yuan, D.X., Jiang, Y.J., Shen, L.C., et al., 2016. Modern Karstology. Science Press (in Chinese).
Zarei, M., Raeisi, E., Merke, B.J., Kummer, N.A., 2013. Identifying sources of salinization using hydrochemical and isotopic techniques, Konarsiah. Iran. Environ. Earth Sci. 70 (2), 587–604. https://doi.org/10.1007/s12665-012-2143-8.
Zeng, M., 2012. Study on the distribution and genesis of hot springs in Chongqing. Chengdu Univiversity of Technology. https://doi.org/10.1007/s12665-018-8004-3 (in Chinese with English abstract).
Zhang, Y.L., Pu, D.L., 2005. A geothermal resource exploration and evaluation report of Qiaokouba Huaxin Hot Spring. Baijie Town, Banan District, Chongqing (in Chinese).
Zhang, Y.L., 2006. Detailed investigation and evaluation report of Baiyun Lake geothermal water resources in Qinggang Town. Bishan County, Chongqing (in Chinese).
Zhang, Y., Yang, P.H., Wang, J.L., et al., 2015. Research progress of Hot springs in Chongqing. Carsologica Sinca 34 (5), 468–478. https://doi.org/10.11932/karst20150507 (in Chinese with English abstract).
Zhou, X.L., Li, X.Y., Zeng, Y.S., 1980. Regional hydrogeological survey report in Qianjiang (plotting scale 1:200,000) (in Chinese).
Zhou, X., Li, C.J., Ju, X.M., Du, Q., Tong, L.H., 1997. Origin of subsurface brines in the Sichuan Basin. Ground Water 35, 53–58. https://doi.org/10.1111/j.1745-6584.1997.tb00060.x.
Zhou, X., Cao, Q., Li, S.P., Wang, L.D., et al., 2014. The formation of Ningchang Salt spring in Wuxi County. Chongqing. Quatern. Sci. 34 (5), 1036–1043. https://doi.org/10.3969/j.issn.1001-7410.2014.05.12 (in Chinese with English abstract).
Zhou, S.B., Chen, S.Y., Zeng, M., Li, Y.J., 2017. Research and evaluation on formation mechanism and exploration risk of fault–type geothermal water resources in southeast Chongqing (in Chinese).
Zhou, X., Wang, X.C., Han, J.J., et al., 2018. Evolution of the Subsurface K-Rich Brines in the Triassic Carbonates in the Sichuan Basin of China. Ground Water 56 (5), 832–843. https://doi.org/10.1111/gwat.12614.